The Astrophysical Journal, 985:39 (17pp), 2025 May 20 https://doi.org/10.3847/1538-4357/adc112

Multiwavelength Long-term Studies of Radio Galaxy NGC 1275

Vera G. Sinitsyna and Vera Y. Sinitsyna
P. N. Lebedev Physical Institute, Russia; sinits@sci.lebedev.ru
Received 2023 August 2; revised 2025 February 27; accepted 2025 March 9; published 2025 May 13

Abstract

It is widely considered that the processes of an interaction between the energy and radiation, which are generated in the active galactic nuclei (AGN) by accretion onto their central massive black hole with the gas in the host galaxy, take a great part in the evolution of the galaxies at all development stages. Such "feedback" of the galaxy environment by AGN including the role of their jetted outbursts generally has no evidence through the multiwavelength observations. Only a few objects are suitable for these purposes. The Perseus cluster of galaxies with the central galaxy NGC 1275 is a perfect laboratory for studying both the physics of AGN's relativistic jets and the feedback role of the central galaxy. Here, the most complete long-term observations across the electromagnetic spectrum from radio up to very-high-energy gamma rays are collected. The multiwavelength light curve provides evidence for the variability of NGC 1275 on decade timescales in the whole energy range and points to the connection of the observed activity with the launch of the features of the relativistic jets from the NGC 1275 core. The relation of multiwavelength emission components is demonstrated with spectral energy distribution and emission maps of the central part of the Perseus cluster. The evidence of the interaction of cosmic rays and magnetic fields generated in the jets at the galactic center with the gas of the Perseus cluster is obtained.

Unified Astronomy Thesaurus concepts: Galaxy jets (601); Seyfert galaxies (1447); Galaxy clusters (584)

1. Introduction

Investigations of galaxy clusters hosting active galactic nuclei (AGN) are of great importance as the role of the AGN and the activity of their central black hole in "feedback" and the evolution of surroundings is not clear now (see, e.g., B. R. McNamara & P. E. J. Nulsen 2012; and A. C. Fabian et al. 2015 for reviews). Also, the study of the emission associated with central regions of AGNs provides valuable information about the relativistic outflows or jets, which are the characteristic features of wide mass-range black holes from stellar-mass galactic ones (A. A. Zdziarski et al. 2012; K. I. I. Koljonen et al. 2018; V. G. Sinitsyna & V. Y. Sinitsyna 2022) up to the supermassive black holes (SMBH) in the AGNs (S. G. Jorstad et al. 2010, 2013). It is believed that large-scale shocks as well as galactic wind or central AGN within these objects accelerate protons and electrons, which are producing very-high-energy gamma-ray emission (B. Dennison 1980; B. P. Houston et al. 1984; H. Böhringer et al. 1993; S. Colafrancesco & P. Blasi 1998; C. L. Sarazin 1999; F. T. Miniati et al. 2001; A. N. Timokhin 2004; A. C. Fabian et al. 2006; S. Colafrancesco & P. Marchegiani 2009). Thus, such galaxy clusters are widely considered as a possible source of gamma rays of MeV to TeV energies. This gamma-ray emission can be a combination of diffuse and pointlike emission having different spatial and spectral properties. The Perseus cluster is an excellent example of such an object because of its relative proximity (its distance is $\sim$100 Mpc or redshift $z = 0.0179$, M. Strauss et al. 1992); also, it is of extraordinary brightness. It is one of the intensively studied clusters across the electromagnetic spectrum from radio up to high-energy gamma rays. NGC 1275 is a dominant galaxy in the Perseus cluster, which hosts a powerful AGN responsible for most of the features visible through all wavelengths of the electromagnetic spectrum. This object located in the very center of the Perseus cluster has taken on great interest for a long time as a prototype of AGN "feedback" within the galaxy cluster and as a perfect "laboratory" for the study of the jet features reflecting the processes occurring near AGN black hole (J. S. Gallagher 2009).

Depending on the features detected in the different parts of the electromagnetic spectrum, the galaxy NGC 1275 has been classified in various ways. For example, based on the strong nuclear emission lines observed in its optical spectrum, NGC 1275 is classified as a Seyfert 1.5 galaxy (M. P. Veron-Cetty & P. Veron 1998). However, due to the high and fast flux variability of the continuum emission and its polarization (J. R. P. Angel & H. S. Stockman 1980), it is also related to the class of BL Lacertae objects within the unified model of AGN (B. L. Fanaroff & J. M. Riley 1974; C. M. Urry & P. Padovani 1995). But the existing pieces of evidence (P. Kharb et al. 2010) point to the possible simplification of the mentioned AGN unification scheme.

In the radio and X-ray energy range, NGC 1275 is a bright and complex object. In the radio, NGC 1275 contains the bright radio object, known as Perseus A or 3C 84, having an extremely luminous and compact core and extended jets, which have been well studied with very long baseline interferometry (VLBI). This morphology viewed in the radio wavelength is typical for the Fanaroff–Riley I radio galaxy (R. C. Vermeulen et al. 1994; G. B. Taylor & R. C. Vermeulen 1996; K. Asada et al. 2006, 2009). The infrared observations revealed the SMBH of the mass of $3.4 \times 10^8 M_\odot$ (R. J. Wilman et al. 2005) at the center of NGC 1275 AGN. The analysis of the jet precession in NGC 1275 (F. K. Liu & X. Chen 2007) interprets the different scenarios for the merger between two galaxies that resulted in the NGC 1275 object. Extending to great distances, radio emission demonstrates an interaction with the gas inside the Perseus cluster of galaxies. The observational evidence of that interaction and the feedback of the nucleus of NGC 1275

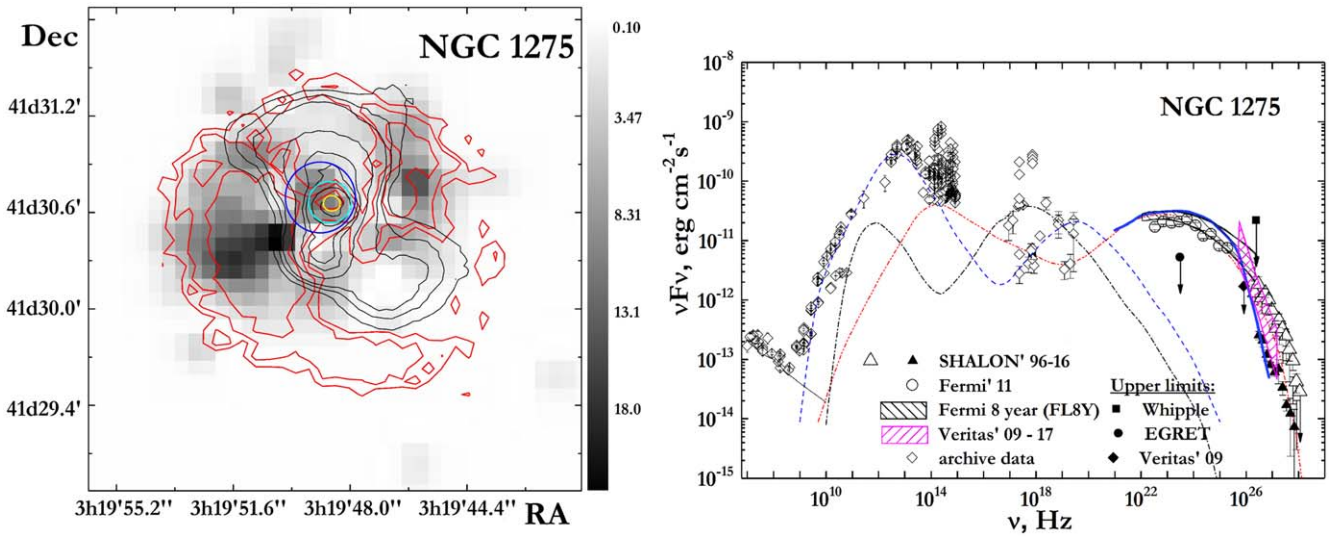

Figure 1. Left: The significance map of NGC 1275 by SHALON in the energy range 800 GeV–55 TeV (gray scale); blue circle shows the position of the emission component within the ∼32″; the red contours indicate the image of NGC 1275 in X-ray (1.5–3.5 keV) by Chandra (A. C. Fabian et al. 2000). Cyan circle corresponds to the contribution of the NGC 1275 nucleus seen in X-rays (H. Böhringer et al. 1993; A. C. Fabian et al. 2000). Contour levels are 55%, 60%, and 75% of the X-ray emission map maximum; the black contours are the radio structures by VLA (332 MHz; A. Pedlar et al. 1990), and the levels correspond to 0.25%, 0.5%, 0.75%, 1.25%, 2.5%, 5%, 12%, and 50% of the maximum. Yellow circle demonstrates the emission viewed in radio 332 MHz from the core of NGC 1275 (A. Pedlar et al. 1990). Right: Spectral energy distribution of the γ-ray emission from NGC 1275. Radio to optical archival data are taken from the NASA/IPAC Extragalactic Database (NED), and X-ray data are from SSDC databases. △ and ▲ represent the data from the SHALON Cherenkov telescope (see text) in comparison with experimental data from Fermi-LAT (2009–2011; A. M. Brown & J. Adams 2011) and the FL8Y–8 yr catalog; EGRET (D. J. Thompson et al. 1995; O. Reimer et al. 2003); Whipple (J. S. Perkins et al. 2006); VERITAS (2009–2017; V. A. Acciari et al. 2009; L. Forston 2019). The dashed, dashed–dotted, and dashed–dotted with two-dot curves indicate the spectral energy distributions of NGC 1275 obtained in the Cannon Model or CM model (S. Colafrancesco et al. 2010), and blue line at high energies is the one-zone model from K. Tanada et al. (2018; see text below).

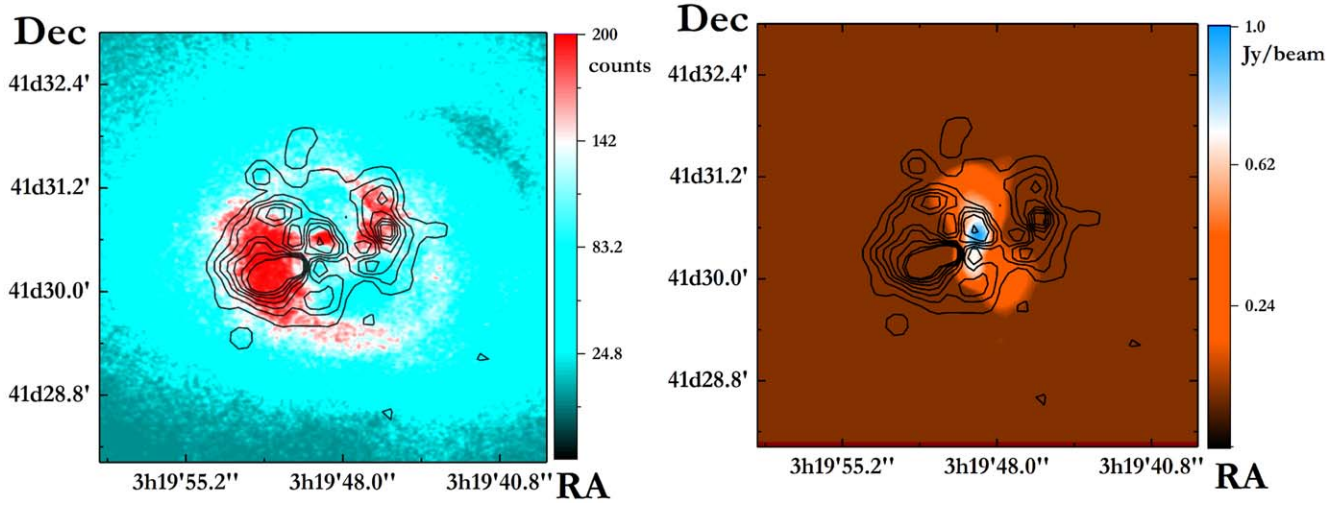

Figure 2. Left: Chandra X-ray (0.1–2.4 keV) image of NGC 1275 (A. C. Fabian et al. 2000). Color scale units are counts. The contours present the sources' TeV structure from SHALON observations at >800 GeV. The black lines display 1σ, 3σ, 5σ, 7σ, 9σ, 11σ, and 13σ confidence level contours. Right: The NGC 1275 radio structure from VLA radio observations. Color scale units are Jy beam^{-1}. The black lines show TeV structures at >800 GeV with 1σ, 3σ, 5σ, 7σ, 9σ, 11σ, and 13σ confidence level contours. The radio and X-ray emission maxima coincide with the active galactic nucleus NGC 1275, while the X-ray emission disappears almost completely near the bright areas of the radio components.

came from studies of the center of the Perseus cluster consistently from ROentgen SAtelite (ROSAT; H. Böhringer et al. 1993) and Chandra (A. C. Fabian et al. 2006) X-ray telescopes (XRTs), which detected the "holes" in the X-ray emission inside of the cluster, which are associated with radio-lobe structures (Figures 1, 2). It suggests that the jets from the central engine of the black hole of the bright radio source 3C 84 blow the numerous "bubbles" into the surrounding intracluster gas of the Perseus cluster (see H. Böhringer et al. 1993 for description).

Meanwhile, the jets are also the target for the detailed investigations of AGNs like NGC 1275 at the short scales as they testify the processes occurring in the vicinity of SMBHs. To study the mechanisms of jet formation and propagation from the very core of AGN, the analysis of long-term observations is used. One of the approaches to such studies is to detect the launching of jet components viewed in the radio range and then link it with flaring events detected at higher-energy ranges. Tracking the jet-initiated variability events through the multiwavelength observations from radio

frequencies up to high-energy gamma rays allows first to resolve the nucleus structure by the determination of the dynamics of the features of the jet flow in the AGN core region (G. F. Paraschos et al. 2022). Whereas the cross identification of the jet features through the wide energy range and the revealing of the time-dependence of the evolution of these jet events allows locating the regions responsible for the generation of observable features, which can lead to exploration of the mechanism of jet launching (see, e.g., G. F. Paraschos et al. 2023) as well as the origin of emission in the AGN.

Investigations of the Perseus cluster as well as the NGC 1275 central galaxy in the high-energy range that got an upper limit of the flux from this object were performed in early experiments on board satellites aiming to search for the sources of gamma-ray emission. First observations were taken with Cosmic Origins Spectrograph (COS)-B mission in the late 70s, from 1975 to 1979 (A. W. Strong & G. F. Bignami 1983), which revealed the excess of gamma-ray emission at energies >70 MeV. But then in 1995, only an upper limit for emission from the Perseus cluster was given at an energy >100 MeV by EGRET (D. J. Thompson et al. 1995). In observations started in 2008, NGC 1275 was detected by Fermi-Large Area Telescope (LAT) as a source of high-energy gamma rays with a flux of an order of magnitude higher than reported by EGRET. Upper limits on the very-high-energy gamma-ray emission from NGC 1275 were obtained in different years in ground-based experiments, such as the large-area scintillation Tibet Array at $E > 3$ TeV (1999; M. Amenomori 1999), and at the Cherenkov telescopes Whipple (2006; J. S. Perkins et al. 2006) at energies >400 GeV, MAGIC (2009; J. Aléksic et al. 2010) at $E > 100$ GeV, and VERITAS (V. A. Acciari et al. 2009) at $E > 188$ GeV in 2009. The extension of the spectral energy distribution data from NGC 1275 up to very-high energies is important for understanding the emission generation processes in the entire energy range.

Here, in this paper, we present the results of long-term studies of the AGN of NGC 1275 object and its surroundings through the wide range of the electromagnetic spectrum including the data obtained in observations at very-high energies started in 1996 (V. G. Sinitsyna et al. 2020) as well as the experimental approach for probing of the mechanisms describing the overall spectral energy distribution data in clusters of galaxies and hosted AGNs.

2. Multiwavelength Observations

The investigation of NGC 1275 emission and its possible origin involve broadband long-term observation data from radio to high energies listed below including the information about spatial flux correlations and connections in flux and spectral variations on the different timescales.

2.1. VLA

Very Large Array (VLA) radio astronomy observatory consisting of 28 25 m parabolic dish antennas, which is used in different configurations, has 74 MHz–43 GHz frequency coverage. VLA observations at 90 cm (332 MHz) with the A and B configuration at a resolution of $\sim 5''$ (A. Pedlar et al. 1990), which are carried out in 1986, and later investigations of 2014 with an upgraded installation at 270–430 MHz with a resolution of $\sim 3\overset{''}{.}6$ (M. Gendron-Marsolais et al. 2020) revealed the inner lobe with loop-like structures, which completely fill the inner X-ray cavities.

2.2. SMA

The Submillimeter Array (SMA) is a radio interferometer consisting of eight radio telescopes that covers the frequencies from 180 GHz (1.67 mm) to 418 GHz (0.717 mm; M. A. Gurwell et al. 2007). SMA has operated since late 2002, and NGC 1275 has been regularly observed with SMA at 1.3 mm and 870 μm resulting in the long-term light curve, which can be used for the detailed flux comparison and for the tracing for the trend of the emission activity behavior.

2.3. The Metsähovi Data

The observations with Metsähovi radio observatory were conducted with a 14 m radio telescope at 37 GHz since 1974. The data about NGC 1275 fluxes collected during this long-term period form a multidecade light curve (see Section 3.2). A detailed description of the Metsähovi experimental technique and data is given in H. Teräsranta et al. (1998).

2.4. ROSAT

ROSAT High Resolution Imager (HRI) is a soft XRT that covers the energy range 0.1–2.4 keV with $38'$ field of view (FOV) and a high spatial resolution of 1.7 ($\sim$2) arcseconds (FWHM). ROSAT observations were carried out in the period 1990–1999 that corresponded to the period of decreased activity in NGC 1275 core, visible as a global minimum in the radio light curve (37, 90 GHz). The X-ray fluxes of NGC 1275 emission in 1991, 1994, 1996, 1997 were extracted in A. C. Fabian et al. (2015) for the long-term X-ray light curve (Section 3.2). The ROSAT HRI observations of the central part of the Perseus cluster show the complicated structures of the X-ray surface brightness within the $5'$ around NGC 1275 galaxy, which is linked with jet activity in radio.

2.5. Chandra

Chandra X-ray Observatory is a high-resolution XRT operating in the overall energy range $0.08 < E < 10$ keV. Chandra Observatory was launched in 1999 and during all that time due to the high resolution with a point-spread function better than $\leqslant 0\overset{''}{.}5$ is producing subarcsecond X-ray images. In particular, the deep Chandra observations of the Perseus cluster revealed two, bubble-shaped cavities extending north and south of the SMBH at the center of the NGC 1275 galaxy (A. C. Fabian et al. 2000). An image of the 0.3–1.5 keV emission from the central regions of the Perseus cluster ($\sim 5\overset{'}{.}5$) is shown in Figure 1 with red lines.

2.6. Swift (UVOT), Swift XRT, Swift BAT

Swift Observatory in space consisting of three instruments aimed primarily to multiwavelength studies of the gamma-ray bursts in the optical, ultraviolet, soft, and hard X-ray energy ranges has been operating since 2005. It provides the X-ray data for all the periods of the NGC 1275 radio intensity increase.

Swift Ultraviolet Optical Telescope (UVOT) is a modified Ritchey–Chrétien telescope with $17'$ FOV and point-spread function of $\sim 2\overset{''}{.}5$. Swift UVOT has six filters that provide observations in three optical (UVV, UBB, UUU) and three UV

(UVW1, UVM2, and UVW2) filters covering the wavelength range 170–650 nm. The fluxes of UVW1 and UVW2 emission associated with NGC 1275 AGN are obtained in F. Imazato et al. (2021) for the overall light curve.

Swift's XRT is a focusing XRT with ∼23′ FOV and ∼18″ resolution (half-power diameter), with X-ray sensitive CCD covered 0.2–10 keV energy range. The XRT has a low-rate photon-counting (PC) mode and a fast-rate windowed-timing (WT) mode. Extracted fluxes for both PC and WT modes are used for the light-curve analysis.

Swift Burst Alert Telescope (BAT) is a wide-FOV of ($100^\circ \times 60^\circ$ or 1.4 sr), coded-aperture instrument with a CdZnTe detector plane operating over the 15–150 keV energy range with a point-spread function of ∼22′. The year-binned light curve of emission associated with NGC 1275 was extracted in F. Imazato et al. (2021) and presented in Section 3.2.

2.7. Suzaku

Suzaku X-ray Imaging Spectrometer (XIS) system on board Suzaku satellite consisting of four X-ray sensitive CCDs optimized for the detection in the energy range 0.2–12 keV. It has 18′ FOV and ∼2′ resolution. Suzaku XIS operated from the mid of 2005 up to 2015, over all the periods of NGC 1275 was used as a calibration target, so it was repeatedly observed with Suzaku every half year (S. Yamazaki et al. 2013; Y. Fukazawa et al. 2018). As a result, the light curve of NGC 1275 at energies 5–10 keV was obtained in Y. Fukazawa et al. (2018) for the period of the raising radio intensity of the NGC 1275 nucleus.

2.8. Fermi-LAT

The space-based gamma-ray detector LAT on board Fermi satellite is a pair conversion instrument sensitive to photons in the energy range from 20 MeV to more than 300 GeV. The LAT has a large effective area of about 9000 cm^2 (at 10 GeV) and an FOV of ∼2.4 sr. The containment radius is $\Theta_{68} = 3.^\circ5$ for $E > 100$ MeV and $\Theta_{68} = 0.^\circ15$ for $E > 10$ GeV. The detector description is given in W. B. Atwood et al. (2009). Fermi-LAT was launched in August of 2008 and has collected the entire sky survey, including the long-term data about NGC 1275 (F. Acero et al. 2015; M. Ackermann et al. 2016). The spectral energy distributions of NGC 1275 averaged over the different periods of activity from Fermi-LAT observations of 2009–2011 and from FL8Y to 8 yr catalog are presented in Figure 1, right. The Fermi-LAT GeV gamma-ray data of NGC 1275 observations from Goddard Space Flight Center[1] were used to obtain the year-binned fluxes for the light curve in the wide energy range (see Section 3.2).

2.9. SHALON

The SHALON telescope system is high-altitude (3340 m above sea level, Tien-Shan mountains, Kazakhstan) imaging Cherenkov telescopes for the 800 GeV–100 TeV gamma-ray astronomy (S. I. Nikolsky & V. G. Sinitsyna 1989; V. G. Sinitsyna 1993; V. G. Sinitsyna & V. Y. Sinitsyna 2011; N. I. Moseiko et al. 2020; V. G. Sinitsyna et al. 2018, 2020). It has the sensitivity to detect a pointlike source at 5σ (T.-P. Li & Y.-Q. Ma 1983) for 50 hr of observation with an integral flux of 2.1×10^{-13} cm^{-2} s^{-1} at the energy of 1 TeV (see details in V. G. Sinitsyna & V. Y. Sinitsyna 2014; V. G. Sinitsyna et al. 2018, 2020) and an angular resolution of $\sim 0.^\circ07$, which is improved by a factor of ∼10 after additional processing (V. G. Sinitsyna & V. Y. Sinitsyna 2014; V. G. Sinitsyna et al. 2018) using the deconvolution algorithm (A. V. Goncharskii et al. 1985). An angular resolution in the gamma-ray astronomy is tightly connected with the accuracy of the reconstruction of the coordinates of the gamma-ray shower source. In SHALON experiment, the information from the shower image shape is used for the determination of the location of the gamma-ray shower source. Since the elongated image of gamma-ray shower by the side with the maximum intensity points toward their source, as a first step, its coordinates can be found through the shower image parameters reflecting the shower elongation and distance from the source. Also, the limit on the size of a gamma-ray source can be set. Parameter dependencies for the coordinate determination and their accuracies, corresponding to the variances of Gaussian point-spread function, can be found in V. G. Sinitsyna & V. Y. Sinitsyna (2014). The accuracy of the determination of gamma-ray position within the emission map acquired using this method is $\sim 0.^\circ07$. Then, an improvement of the angular resolution by a factor of ∼10 is achieved using the deconvolution algorithm (A. V. Goncharskii et al. 1985). Considering the distribution obtained with the above method as being the result of the convolution of the sought-after gamma-ray intensity distribution with the point-spread function, the solving of the inverse problem following A. V. Goncharskii et al. (1985) under the additional assumptions leads to refining of the emission map. The image deconvolution for the gamma-ray sources having high collected statistics with the assumption that the solution is a smooth nonnegative upper-bounded function, and lies within the region determined at the first step can result in the improvement of the angular resolution to further define the object structure.

Under the SHALON program of long-term studies of extragalactic sources at TeV energies (V. G. Sinitsyna 1995, 1996), observations of NGC 1275 Seyfert galaxy were started in 1996. SHALON observations yield the detection of very-high-energy γ-ray emission from NGC 1275 (V. G. Sinitsyna 1997, 2000; Figures 1, 2). Since 1996, NGC 1275 and its surroundings have been intensively investigated by SHALON telescope (V. G. Sinitsyna 1997; V. G. Sinitsyna et al. 1999; V. G. Sinitsyna 2000, 2006; S. I. Nikolsky & V. G. Sinitsyna 2003, 2004; V. G. Sinitsyna et al. 2007, 2009, 2011; V. G. Sinitsyna & V. Y. Sinitsyna 2013, 2014). The 289.8 hr of moonless observations at the zenith angle range 3°–33° were collected in the different years from 1996 to 2016 (see Section 3.2). TeV gamma-ray emission from NGC 1275 was detected by the SHALON telescope above 800 GeV at the 33.7σ determined according to Li–Ma method (T.-P. Li & Y.-Q. Ma 1983) with the averaged integral flux of $I(>0.8\ \mathrm{TeV}) = (7.8 \pm 0.5) \times 10^{-13}$ cm^{-2} s^{-1}. The differential gamma-ray energy spectrum in the observed energy range above 0.8 TeV can be described by a power law with the photon index $k_\gamma = -3.02 \pm 0.14$. Also, the shape of SHALON differential spectrum of gamma rays from NGC 1275 in the energy range from 0.8 to 55 TeV is well fitted with a power law with an exponential cutoff: $dF/dE = (6.9 \pm 0.09) \times 10^{-13} \times E^{-2.61\pm0.16} \times \exp(-E/(28 \pm 9)\mathrm{TeV})$ cm^{-2} s^{-1} TeV^{-1} with χ^2/degrees of freedom (DoF) = 0.94 (with DoF = 9). The spectral energy distribution of the γ-ray emission from

[1] https://fermi.gsfc.nasa.gov/ssc/data/access/lat/msl_lc/

NGC 1275 is shown in Figure 1, right with open triangles (△). Details of the spectral energy distribution of NGC 1275 by SHALON are presented in Table 1 of Appendix A.

TeV structures of NGC 1275 at energies of 800 GeV–55 TeV by SHALON are presented in Figure 1, left with the gray-scale image and in Figure 2 with contours. The color scale in Figure 1 is in units of significance.

The correctness of background evaluation and rejection is confirmed with the distribution of Li–Ma significance values of the background regions out of the source area from Figure 1, left. In the case of correct background evaluation and rejection, it should be distributed as the Gaussian with zero mean value and a width of 1 in the case of correct background estimation (T.-P. Li & Y.-Q. Ma 1983), which is illustrated in Figure 3.

3. Results

In order to find the mechanisms of emission generation in the NGC 1275 object and evaluate the models describing them, the searches for correlation of the emission regions and connection between flux and spectral variations in the wide energy range including radio, X-rays and MeV-TeV γ-rays were performed.

3.1. Structures and Spectral Energy Distributions of NGC 1275

The structure of the Perseus cluster centered on NGC 1275 in both X-rays by ROSAT HRI and radio by VLA (332 MHz) were overlaid and analyzed in H. Böhringer et al. (1993). Both a bright central peak emission in soft X-ray with the radius of $\sim 10''$ (see cyan circle in Figure 1, left; and H. Böhringer et al. 1993; A. C. Fabian et al. 2000) and the radio 332 MHz intensity within $\sim 8''$ size (see yellow circle in Figure 1, left; and A. Pedlar et al. 1990) originate from the location of the AGN of NGC 1275. The X-ray brightness minima are located to the north and south of the described central bright spot (Figure 2, left) and correspond to the position of radio lobes detected in VLA observations (Figure 2, right).

We combined very-high-energy emission map of NGC 1275 visible at 0.8–55 TeV by SHALON with ones in X-rays viewed by Chandra (A. C. Fabian et al. 2000) and radio detected by VLA (A. Pedlar et al. 1990; see Figures 1, 2). In Figure 1, left, the TeV image by SHALON (gray scale) is overlaid with 332 MHz VLA contours (black contours) and 1.5–3.5 keV Chandra X-ray data (red lines). In Figure 2, X-ray structure and radio image are presented with color, but TeV significance map from SHALON observations is shown with black lines. The emission regions of very-high-energy gamma rays from NGC 1275 and its surroundings well correlate with the ones visible in X-rays and show the same features. In both X-rays and TeV gamma rays, the images of the Perseus cluster center demonstrate a circular symmetric structure with the clear peak emission from the position of NGC 1275 core (see cyan and blue circles in Figure 1. left). The prominent X-ray surface brightness maxima around the core coincides with maxima of TeV flux to the east of the nucleus of NGC 1275 and TeV flux excess at the west. The clearly seen minima both in the X-ray surface brightness and in the TeV gamma-ray fluxes to the north and south from NGC 1275 overlap with outer radio lobes (black lines), which are further surrounded with bright X-ray arc regions. The explanation of the observed relation of X-ray and radio structures is that the bright arc-shape X-ray emission comes from the X-ray radiated gas shells surrounding the radio

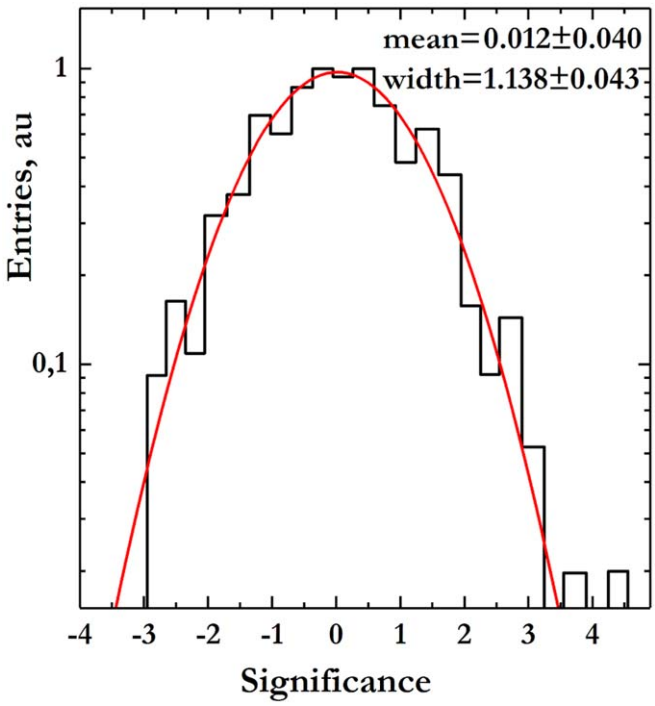

Figure 3. Distributions of significance in the FOV out of source area during the observations of NGC 1275. The red curve illustrates the expected normal Gaussian distribution.

lobes (A. C. Fabian et al. 2000). A region of bright emission is detected to the west from the nucleus.

So, the very-high-energy gamma-ray emission regions around NGC 1275 detected by SHALON have a configuration similar to one visible on X-rays (see also A. C. Fabian et al. 2000) and match well with the emission regions viewed in the photons of 1.5–3.5 keV energies (Figure 1, left and Figure 2, left). A spatial correlation between the emission regions of very-high-energy gamma rays of 0.8–55 TeV (S. I. Nikolsky & V. G. Sinitsyna 2003; V. G. Sinitsyna et al. 2007, 2009) and X-rays of the 0.3–7 keV (A. C. Fabian et al. 2000) was found. Namely, the image of NGC 1275 viewed in TeV gamma rays by SHALON has an extended structure with the spot of emission centered at the AGN core location (blue circle in Figure 1, left). Additionally, to study the emission of NGC 1275 related to the activity of the black hole, the component corresponding to the peak of gamma-ray intensity from the position around the NGC 1275 core was extracted. Given the SHALON angular resolution achieved in the case of full data collected in the NGC 1275 observations, the central emission component of $\sim 32''$ (marked with blue line circle in Figure 1) was used for the further analysis. Very-high-energy gamma-ray emission of energies >0.8 TeV from this compact source of emission was detected at a confidence level of 13.5σ (method T.-P. Li & Y.-Q. Ma 1983) with a value of average integral flux of $(3.26 \pm 0.30) \times 10^{-13}\,\mathrm{cm}^{-2}\,\mathrm{s}^{-1}$. And this source can be associated with the contribution of the unresolved in the details at the TeV energy nucleus of NGC 1275. The differential gamma-ray emission energy spectrum of the extracted compact component was obtained. A power law with exponential cutoff that fits the data points in the energy range from 0.8 to 40 TeV $dF/dE = (2.02 \pm 0.11) \times 10^{-13} \times E^{-2.52\pm0.10} \times \exp(-E/(10 \pm 2)\ \mathrm{TeV})\ \mathrm{cm}^{-2}\,\mathrm{s}^{-1}\,\mathrm{TeV}^{-1}$ describes well the observed spectrum. The

spectral energy distribution of the emission from the component corresponding to the contribution of the nucleus of NGC 1275 by SHALON is presented in Figure 1, right with the black triangles (▲). Details of the spectral energy distribution of the emission component within the ∼32″ by SHALON are presented in Table 2 of Appendix A.

At high energies of 100 MeV–300 GeV, NGC 1275 was detected by the Fermi-LAT experiment (A. A. Abdo et al. 2009), and has been intensively studied since then. The MeV–GeV gamma-ray spectrum obtained for the 8 yr of observations since 2008 has a higher flux than that reported in A. M. Brown & J. Adams (2011; see black-dash-filled area and open circles in Figure 1, right). Recently, the detection of the emission at energies of 150 GeV up to >1 TeV from NGC 1275 in the different states was reported by the VERITAS mirror Cherenkov telescope based on the 8 yr observations (L. Forston 2019).

Figure 1, right compares the average spectral energy distributions of NGC 1275 (△) and its central region of ∼32″ (▲) obtained from SHALON data (1996–2012, 2015, 2016; V. G. Sinitsyna & V. Y. Sinitsyna 2014) with the Fermi-LAT (2009–2011; A. M. Brown & J. Adams 2011) and the FL8Y–8 yr catalog[2] and with the mean flux by VERITAS (2009–2017; L. Forston 2019) together with other experimental data (D. J. Thompson et al. 1995; J. S. Perkins et al. 2006). Also, in the broadband spectral energy distribution of Figure 1, the NASA/IPAC Extragalactic Database (NED)[3] radio to optical data and Space Science Data Center[4] (SSDC) X-ray data are presented.

3.2. Multiwavelength Variability of NGC 1275 and Connection of Very-high-energy Flares with Jet Features

NGC 1275 is known to be a highly variable object demonstrating both dramatic changes in radio flux over the decades and short-timescale activity at optical wavelengths (see, e.g V. M. Lyutyi 1977; K. A. Kingham & R. W. Oconnell 1979). NGC 1275 flux variations and their connection through the broadband energy range show the contribution of the nucleus to the detected changes. For example, the activity detected from the region near the core of the object in the radio energy range, which is referred to as the appearance of the jet features (B. Punsly et al. 2021; G. F. Paraschos et al. 2022), plays an essential role in the generation of the emission over a wide frequency range during the outbursts.

Besides the revealed correlations of the spatial emission features of NGC 1275 in the different wavelength, the study of the changes of the intensity in the wide energy range and on the different timescales will provide the opportunity to investigate the evolution of this object and mechanisms leading to the observed results. For this purpose, the experimental data from the long-term studies at radio, X-rays, high-, and very-high-energies have been collated to reveal possible correlations of the emissions in various energy ranges. In Figure 4, the information about TeV gamma-ray fluxes from SHALON long-term observations of NGC 1275 is combined with the archive light curve at 32–37 GHz (H. Teräsranta et al. 2005; H. Nagai et al. 2012; K. L. Dutson et al. 2014), X-ray data by ROSAT HRI (0.1–2.4 keV) (A. C. Fabian et al. 2015), Suzaku/XIS (5–10 keV; Y. Fukazawa et al. 2018), and Fermi-LAT year fluxes at high energies above 100 MeV (K. Tanada et al. 2018). The red triangles at the upper part in Figure 4 indicate the integral fluxes from the SHALON data at >800 GeV that are averaged over each year of observations. Details of points of year-averaged light curves are provided in Table 3 of Appendix B. In the case of gamma-ray excess, the fluxes obtained from the data are averaged over 3 to 5 days and are shown with the yellow-filled triangles; or else, the monthly averaged points are presented (see details of this light curve in Table 4 of Appendix B). The fluxes of the emissions indicated at the right axes of Figure 4 are presented in arbitrary units.

Comparing the TeV gamma-ray light curves with ones viewed at radio, X-rays, and high-energy gamma rays allows to trace the long-term behavior of NGC 1275 intensity and possible conditions of the "switching-on/off" of activity. Whereas the relation of the short-range flaring events at high energies to the appearance of jet features detected at radio frequencies may point at the location of the gamma-ray emission region and the development of the activity of the sites in the center of AGN. For the study of the NGC 275 core behavior, the connection of TeV gamma-ray light curve with changes of radio fluxes in the different energy ranges, reflecting the activity of the AGN, and also, with available data at X-rays, is considered. The ejection date of the jet features at 43 and 86 GHz that are supposed to occur in the vicinity of the black hole at the center of NGC 1275 (G. F. Paraschos et al. 2022) is shown in Figure 4 for the purpose of relation to the activity at TeV energy range. Below, the trends of the NGC 1275 fluxes' behavior are presented together with the TeV-flux changes.

The data about TeV gamma rays from NGC 1275 have been collected in SHALON experiment since 1996, and the average integral flux is $(7.8 \pm 0.5) \times 10^{-13}\,\mathrm{cm}^{-2}\,\mathrm{s}^{-1}$. However, during the long-term observations, the intensity of NGC 1275 was found to be variable in the very-high energies (see Figure 4). Thus, in the period 1999–2001, the decrease of the integral flux below the average was detected with the value of $(4.7 \pm 1.3) \times 10^{-13}\,\mathrm{cm}^{-2}\,\mathrm{s}^{-1}$. After this period, the starting of the growth of intensity through the wide energy range was noticed, the activity of NGC 1275 in very-high energies raised as well, and a light curve shows a slow TeV gamma-ray flux increase.

Also, the SHALON telescope has detected five short-time (within 5 days) increases of the TeV γ-ray flux in the entire time of observations of NGC 1275. The increases in TeV-emission flux were detected in late 2001 January, 2003 September, 2005 late November–early December, and late 2009 October. Also, a high level of flux was detected in the mid of 2015 September. The values of fluxes in these periods were $(21.2 \pm 7.5) \times 10^{-13}$, $(14.1 \pm 7.5) \times 10^{-13}$, $(35.5 \pm 12.4) \times 10^{-13}$, $(23.4 \pm 4.5) \times 10^{-13}$, and $(38.6 \pm 10.3) \times 10^{-13}\,\mathrm{cm}^{-2}\,\mathrm{s}^{-1}$, respectively. The flux increase in 2005 November was observed during the 4 days. The duration of the period of the flare in 2009 October was 3 days. But the duration of intervals of the flux increases in 2001 and 2005 December was not found because the observations were interrupted due to weather conditions in both cases.

Considering the detected short-time increases of gamma-ray flux, it can be suggested (J. A. Hodgson et al. 2021) that the flaring activity detected in the gamma rays may be associated with the events of changes in jet morphology on the subparsec scales, namely, with the appearance of the new components of

[2] https://fermi.gsfc.nasa.gov/ssc/data/access/lat/fl8y/
[3] http://ned.ipac.caltech.edu/
[4] https://www.ssdc.asi.it

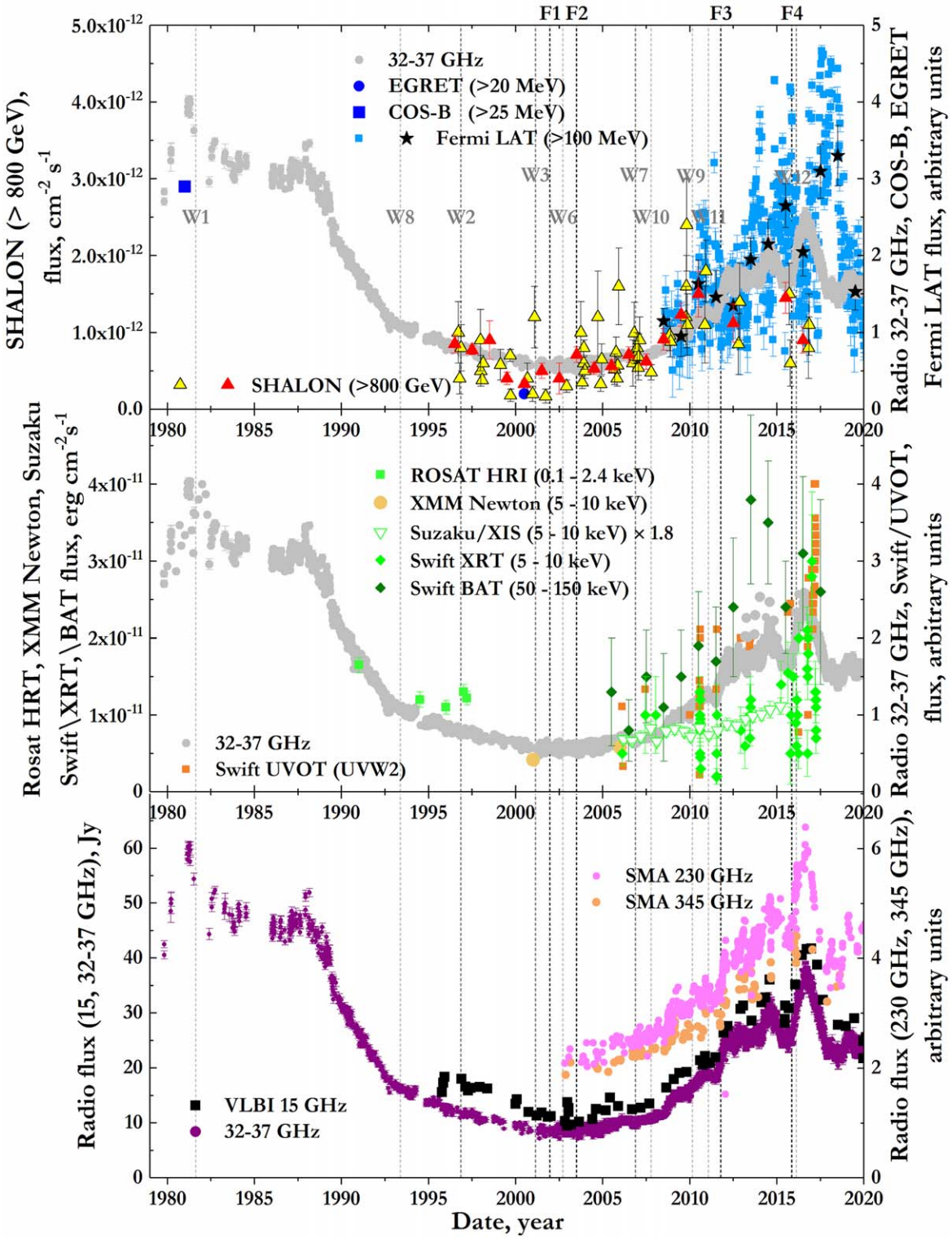

Figure 4. Light curve for NGC 1275 at different energy ranges. It includes Metsähovi data at 32–37 GHz (H. Teräsranta et al. 2005; H. Nagai et al. 2012), Rosat HRI (0.1–2.4 keV; A. C. Fabian et al. 2015), and Suzaku/XIS (5–10 keV; Y. Fukazawa et al. 2018), COS-B (>25 MeV; A. W. Strong & G. F. Bignami 1983), Fermi-LAT (>100 MeV; A. M. Brown & J. Adams 2011; K. Tanada et al. 2018), and SHALON (>800 GeV; V. G. Sinitsyna & V. Y. Sinitsyna 2020). The fluxes are presented in arbitrary units: the UV data are in the units of 9×10^{-27} erg cm^{-2} s^{-1}; the soft X-ray data is in the units of 1.8×10^{-12} erg cm^{-2} s^{-1}; high-energy year fluxes from Fermi-LAT observations, data from COS-B, and EGRET upper limits are in units of 2.0×10^{-7} cm^{-2} s^{-1}; very-high-energy year integral fluxes from SHALON observations (red- and yellow-filled triangles, see text) are in the units of *ph* cm^{-2} s^{-1}.

the radio features. It should be noted that, near the 2001–2003 period and after that, the object has begun brightening in X-rays as well as in the high- and very-high-energy gamma rays (see Figure 4), which corresponds to the appearance of the relativistic jet features (referred to as C1, C2, C3) detected in the radio range of 43 GHz by VLA. The flares of very-high-energy gamma-emission started to record in the period of appearing C1 and C2 jets' components and then during the

separation between C1 and C3 (H. Nagai et al. 2010, 2012; K. Suzuki et al. 2012).

Also, a number of features were identified at 86 GHz (referred to as W see G. F. Paraschos et al. 2022), which started to eject since the 1980s. Out of these raw radio events, W1 feature is found to be coinciding with the total radio flare of the 1980s and is possibly corresponding to C2 component. A part of W features was cross identified with ones detected at 43 GHz (G. F. Paraschos et al. 2022). The dashed lines in Figure 4 show the ejection dates of W and F features together with the points of TeV flux increases (see yellow-filled triangles). The cross-identified components are shown with black dashed lines in Figure 4. The fast moving 86 GHz components were found (G. F. Paraschos et al. 2022); they are marked with dark-gray-dashed lines in Figure 4. A correspondence between the high-level gamma-ray fluxes and the radio features is visible in Figure 4. However, that association can be indirect due to the gaps in sampling of the TeV data points caused by the observational method, and the gamma-ray flux increases might be corresponding with the radio features appearing after or before the detected gamma-flares. The high TeV fluxes were observed within ∼2 yr before the features' appearance.

Also, in Figure 4, the increases of gamma-ray fluxes by SHALON were compared with ones from the lower-energy gamma-ray and X-ray detecting experiments in the periods when the observations were simultaneous. The Fermi-LAT started to collect the data from 2008 August 4 (A. M. Brown & J. Adams 2011; K. Tanada et al. 2018). Only a part of SHALON observation periods, including the flaring ones, can be compared directly with Fermi-LAT data. SHALON observations of NGC 1275 were performed in 2008 November with a break for the Moon's time, 2009 October, 2010 mid-November–early December, and 2015 mid-September to the start of October. In 2009 October 18–20, the γ-ray flux increase to $(23.4 \pm 4.5) \times 10^{-13}\,\mathrm{cm}^{-2}\,\mathrm{s}^{-1}$ was detected. Comparing with Metsähovi light-curve radio data at 37 GHz (H. Nagai et al. 2012), the high TeV fluxes occur at the period from 2009 October to 2009 November with the rise followed by the fall in the flux density on the month timescale. Also, this flare period of 2009 in SHALON observations corresponds to the times of the high hardness ratio in Fermi-LAT data (K. Tanada et al. 2018). The increased fluxes of 2015 coincide with one of the main flares of high-energy γ-rays observed by Fermi-LAT. Figure 4 shows the global trend in the behavior of the light curves viewed from radio to very-high-energy gamma rays, that is the growth of the emission intensity after the 2000–2003 period, but the increase of TeV and X-ray fluxes is not as large as one of the radio and MeV–GeV gamma ray fluxes (K. Tanada et al. 2018).

3.3. Correlation of Multiwavelength Light Curves and Gamma-Ray Emission Location

Apart from the description of light curves and flares at different energies presented above, more detailed examination of the correlations in the temporal evolution of the NGC 1275 intensities at radio, X-rays, and very-high-energy gamma rays is performed to extract the information about the time-dependencies including the time-lags in the observed data and then to constrain possible emission sites.

To probe for the correlations of the measured (at different energy ranges) light curves, including timescales of variability and possible time-lags between the pairs of light curves, a method of the discrete cross correlation function (DCF) is used for the described data. This method was developed by R. A. Edelson & J. H. Krolik (1988) and then is extensively used to find the correlations in the uneven data samples, which can be of different length and with measurement errors known. The full description of DCF analysis method can be found in R. A. Edelson & J. H. Krolik (1988) and also D. R. S. Robertson et al. (2015). If the DCF analysis reveals the correlation with the positive time-lag between two light curves, the features of the first set of data occur before those of the second one. In the case of the negative time-lag, the features of the first light curve appear after the second ones. Here, for the data analysis, we used the implementation of DCF method presented in D. R. S. Robertson et al. (2015). The correlations of TeV gamma-ray light curve to fluxes at different energy ranges, namely, 15, 37, 230, and 345 GHz, and to available data at X-rays, are considered.

The observational time intervals for data sets presented here are supposed to be used further for the searches, for the cross correlations vary at different energy ranges. The light curve of 37 GHz covers multiple decades spanning from 1978 up to 2020. It includes the maximum activity period of ∼1980–1988; the time of fall of intensity at ∼1990–2000 and its minimum at the period of 2000–2005; as well as a rise of intensity in 2006–2012 that is followed by the period of the high activity starting in ∼2012. Whereas the data from SHALON observations at >0.8 TeV and 15 GHz VLBI points cover the similar time interval from 1996 to 2016 and 1995 to 2020, respectively, that includes the periods of flux fall, the intensity minimum, its rise, and the starting of activity. The time range of radio data at 230, 345 GHz is available from 2002 to 2020. The soft X-ray observations were taken with Suzaku and Swift XRT from 2006 to 2020. Thus, collected through the wide energy range, data sets have both different timescales of the light curves and different data sampling (see Figure 4). To minimize possible uncertainties caused by the different observational time ranges and the long-time intervals without data, the cut data set is used for the cross correlation analysis. The data set is limited around the time interval of 1996–2016 containing a common light-curve shape behavior trend used as the main cross correlation feature. For the DCF pairs 15 GHz γ-rays, 37 GHz γ-rays, the radio light curves are limited to the time range 1996–2016, to match the time range of the very-high-energy light curve. Whereas in the millimeter light curve, the data set is limited with the period of 2002–2016. Also, the common period was taken for the analysis of X-ray–γ-ray light curves.

The results of the correlation analysis are presented in Figure 5. The dashed magenta, dashed–dotted red, and dashed–dot–dotted orange lines in Figure 5 are the 68.27% (1σ), 95.45% (2σ), and 99.73% (3σ) confidence levels showing the significance of the peaks. It was determined via simulations of 15,000 light curves using the code of S. Connolly (2015), basing on D. Emmanoulopoulos et al. (2013). The details about the method and key parameters of simulations can be found in C. Chidiac et al. (2016), D. Emmanoulopoulos et al. (2013), and S. Vaughan (2005). As peaks are mostly well above 3σ confidence level (see Figure 5), the radio, X-ray, and TeV gamma-ray fluxes are correlated. The peaks in the cross correlation functions correspond to the time-lags between the light curves. So, the time-lags (τ) were detected between the fluxes observed in the radio and TeV energy range. Namely,

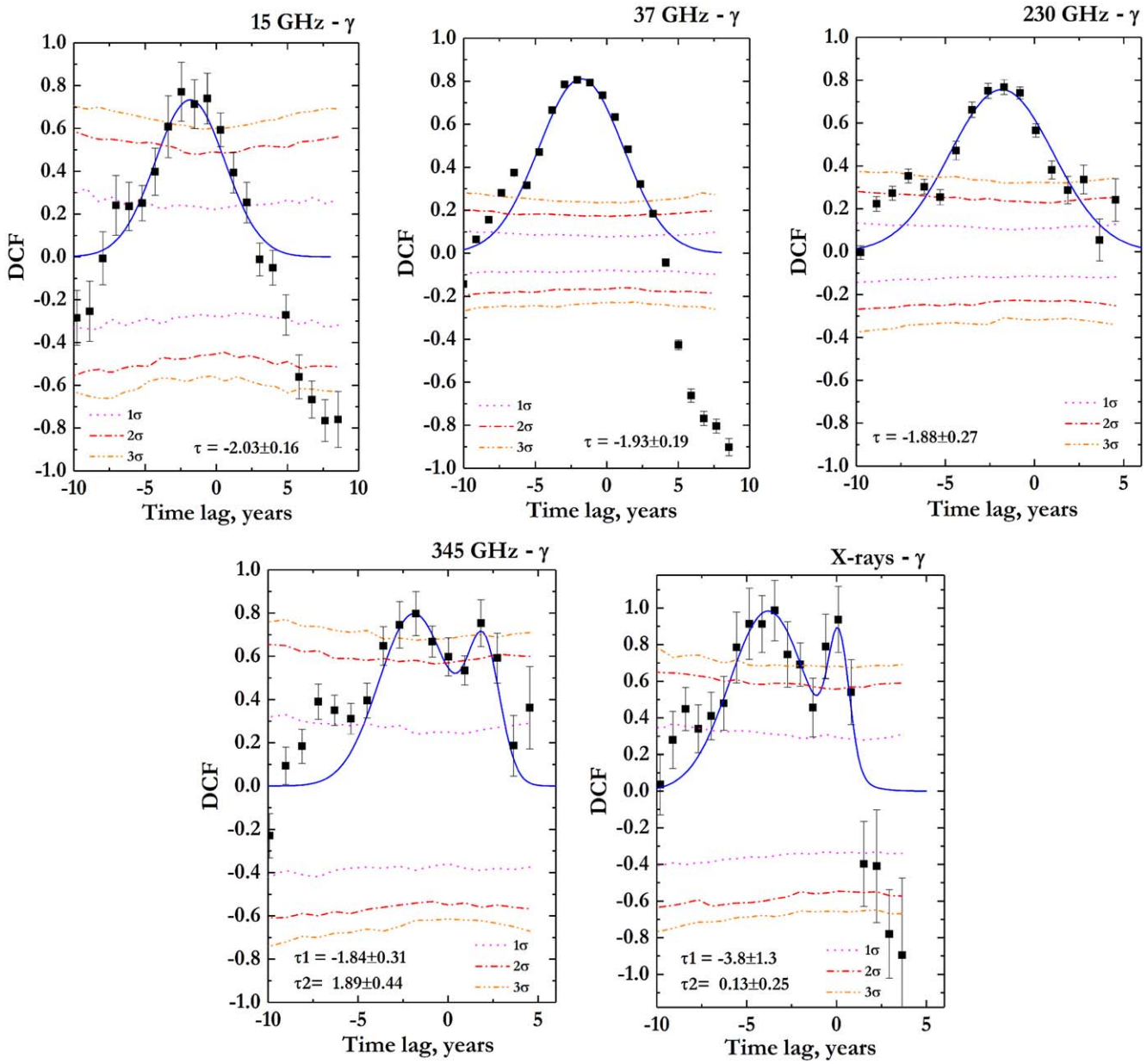

Figure 5. Discrete cross correlation function of light curves: 15, 37.0, 230, 345 GHz, and soft X-rays vs. TeV gamma rays of >800 GeV energy (by SHALON). Results of DCF analysis are presented with black points. The blue line corresponds to a Gaussian or a double Gaussian function fit to the DCF points with the mean value τ corresponding to the peak position. The dashed magenta, dashed–dotted red, and dashed–dotted–dotted orange lines show the 68.27%, 95.45%, and 99.73% confidence band respectively.

$\tau_{15\mathrm{GHz}-\gamma} = -2.09 \pm 0.16$, $\tau_{37\mathrm{GHz}-\gamma} = -1.97 \pm 0.19$, $\tau_{230\mathrm{GHz}-\gamma} = -1.89 \pm 0.27$, $\tau_{345\mathrm{GHz}-\gamma} = -1.84 \pm 0.41$. A weak peak in the correlation function $\tau_{345\mathrm{GHz}-\gamma} = 1.89 \pm 0.44$ was found as well. Also, the significant feature in the 15 GHz γ-ray and 37 GHz γ-ray cross correlation functions is the negative correlation (i.e., anticorrelation) seen at a positive time-lag of 7.65–8.5 yr indicating that the minimum of radio light curves is leading the maximum in the TeV data by ∼8 yr. It is a consequence of both the detected correlation of 15 and 37 GHz radio and gamma-ray data with the time-lag of ∼−2 yr, and, also, the common light-curve behavior trend, which is the growth of the observed intensity from minimum to maximum activity, that takes about 10 yr. The found time-lags are frequency dependent, and the values of their difference at the radio wavelength are consistent with ones obtained in the G. F. Paraschos et al. (2023) for the delays of light curves for the corresponded wavelength.

The time-lags of the X-ray to TeV gamma-ray light curves are $\tau_{\text{X-ray}-\gamma} = -3.8 \pm 1.3$ and $\tau_{\text{X-ray}-\gamma} = 0.12 \pm 0.25$. Here, the negative lag indicates that the variations occur later than gamma-ray ones. The results for the X-rays to gamma-rays time-dependencies with the about 3.8 ± 1.3 yr delay of X-ray data reflect the fact that X-ray flux in the 5–10 keV energy range from Suzaku measurements was nearly constant before 2010–2012 yr and then increased gradually between 2012 and 2015 (Y. Fukazawa et al. 2018), whereas the gamma-ray fluxes start the growth near around 2005–2008 (see Figure 4). This delay may not be connected with the processes related to the activity of NGC 1275 resulting in variations of X-rays but may be caused by the not sufficient sensitivity of Suzaku to the

X-ray flux changes between 2006 and 2012 (I. Edahiro et al. 2015). The same situation may take place with the X-ray data from the Swift experiment (F. Imazato et al. 2021). Some modest correlation of X-ray and gamma-ray data with the zero 0.12 ± 0.25 yr time shift might be a result of the flares simultaneously observed in the X-ray and gamma-ray energy range in the period near 2009, 2010, 2012.

Assuming that light-curve events are connected, and considering an approach where the origin of the observed delay in the light curves is due to the propagation effect based on the energy dependent moments of the leaving from the common source of all-wavelength-emission from the opacity zone around the central black hole (R. D. Blandford & A. Königl 1979; A. A. Königl 1981; R. D. Blandford et al. 2019), the detected time-lags can be converted to the distance between the regions emitting at considering energies (see A. P. Lobanov 1998). The distance from the radio core emission to locations of gamma rays can be expressed following A. B. Pushkarev et al. (2010) and E. V. Kravchenko et al. (2016) through the detected time delay between the observed events of the gamma-ray and radio emission, the redshift, and the apparent jet speed, which is determined from the VLBI observations and the jet viewing angle. For the estimations presented here, the minimum and maximum values of the last two parameters were taken from the detailed analysis of the VLBI observations of NGC 1275 aimed to the extraction of the characteristics of the jet structure (G. F. Paraschos et al. 2021; G. F. Paraschos et al. 2022). It is estimated that the TeV gamma-ray emission site would be shifted upstream from the radio core on about 5.7×10^{-3}–19.6×10^{-3} pc. The position of the radio core region relative to the jet base that is generally considered as a distance to the central black hole engine can be estimated following A. P. Lobanov (1998) through the parameters obtained from the measurements in the radio wavelength. The dedicated analysis, including the extraction of the apparent frequency-dependent core position parameters, depending on the electron energy spectrum and the magnetic field in the emitting region parameter and the jet viewing angle, is performed in G. F. Paraschos et al. (2023) using radio observations at frequencies between 4.8 and 345 GHz. It results also in the estimations of the position of the radio core region at different frequencies. Using the jet features parameters (G. F. Paraschos et al. 2021; G. F. Paraschos et al. 2023) and applying them to the gamma-radio core shift extracted from the detected negative time-lags between radio and gamma-ray light curves, the very-high-energy gamma-ray emission site would be about $(6.7–20.1) \times 10^{-3}$ pc or $(205.1–615.2)R_s$ (where R_s is the Schwarzschild radius). The consideration of the positive time-lag between 345 GHz radio data and gamma-ray fluxes bounds the position of TeV gamma-ray emission region, being about $(40.1–210.5) \times 10^{-3}$ pc or $(1224–6443)R_s$. The radio to gamma-ray delays and the estimated distance are consistent with values presented in G. F. Paraschos et al. (2023) obtained from the analysis of radio and Fermi-LAT gamma-ray light curves.

3.4. Evolution of Spectral Energy Distribution

Since the correlations between the TeV gamma-ray, radio, and X-ray fluxes were found, the spectral behavior of NGC 1275 in the wide energy range was additionally analyzed in the different periods of the activity as identified from the gamma-ray light curve. As the observed gamma-ray intensity follows the overall trend of first the dropping of observed fluxes before 2000 and then of their gradual increase starting from the period of 2003–2008, this study involves the period of minimum intensity in 2000 and then during the rising fluxes up to 2009–2010. This includes the study of the gamma-ray spectral index at energies of >0.8 TeV and available spectral indices in the radio band in the period matching the time of observations at very-high energies. The yearly gamma-ray spectral indices using a simple power-law model were derived and compared with once at 35–90 GHz (see Figure 6, top). Figure 6 presents the time-dependence of indices of gamma-ray and radio spectra in the period 1996–2016 during which the light curves significantly overlap. Figure 6, top shows a similar trend in gamma-ray ($k_{\gamma 0.8-10\mathrm{TeV}}$) and radio ($\alpha_{35-90\mathrm{GHz}}$) spectral behavior regarding hardening of the spectra in the TeV energy range in 2005–2006 that occurs at about 2 yr before one in the 35–90 GHz band. It should be noted that about 2 yr lag in the changing of the radio fluxes relative to gamma-ray ones was reported above as the feature of the correlation of the light curves.

Then, to trace a possible connection of the evolution of overall spectral properties at low and high energies, the multiwavelength spectral energy distribution was constructed for the different times of the activity starting from the period of minimum gamma-ray fluxes observed in 2000 and then during the rising fluxes. In Figure 6, bottom, the bow tie shape areas show available averaged spectral data at radio, X-rays, MeV–GeV gamma rays, and TeV–gamma rays in 2000, 2003, 2006, and 2009. The spectral behavior in the different activity periods is presented together with overall observation data collected for all periods of observation of NGC 1275. The colors of the bow tie areas in Figure 6, bottom correspond to the radio and TeV gamma-ray spectral states from Figure 6, top. X-ray data are presented with nonthermal X-ray emission from Swift XRT and Swift BAT observations of 2008–2010 and 2005–2007 correspondingly and are shown with green and red bow tie areas in Figure 6, bottom.

Although the archival data points from Figures 1, 6 for the overall spectrum collected in the optical band contain host galaxy contamination, the source viewed in X-ray is extended; the nonthermal spectral energy distribution shows two components, one peaking near-IR, and the other around the gamma-ray energy range. The observed shape of the spectral energy distribution is analogous with one of blazars (e.g., S. Inoue & F. Takahara 1996; G. Fossati et al. 1998; H. Kubo et al. 1998) whose low-energy component is caused due to synchrotron radiation of relativistic electrons accelerated within the outflow, and Compton scattering by the same electron is responsible for the nonthermal X-ray and high-energy gamma-ray component (synchrotron self-Compton, hereafter SSC, mechanism). As it suggested from the collected data, the fluxes of the gamma-ray and lower-energy humps are comparable; thus, first, the observed spectral energy distribution is similar to low-frequency-peaked BL Lac objects, and SSC mechanism can be responsible for the emission from the NGC 1275 object (M. Sikora et al. 2009). The one-zone SSC model (A. A. Königl 1981) is widely applied for the description of the blazar emission spectral energy distribution.

Here, a simple one-zone SSC model (A. Tramacere et al. 2009) is used to fit the available data collected for the spectral energy distributions of emission from NGC 1275 at the different states of activity. The model assumes that the

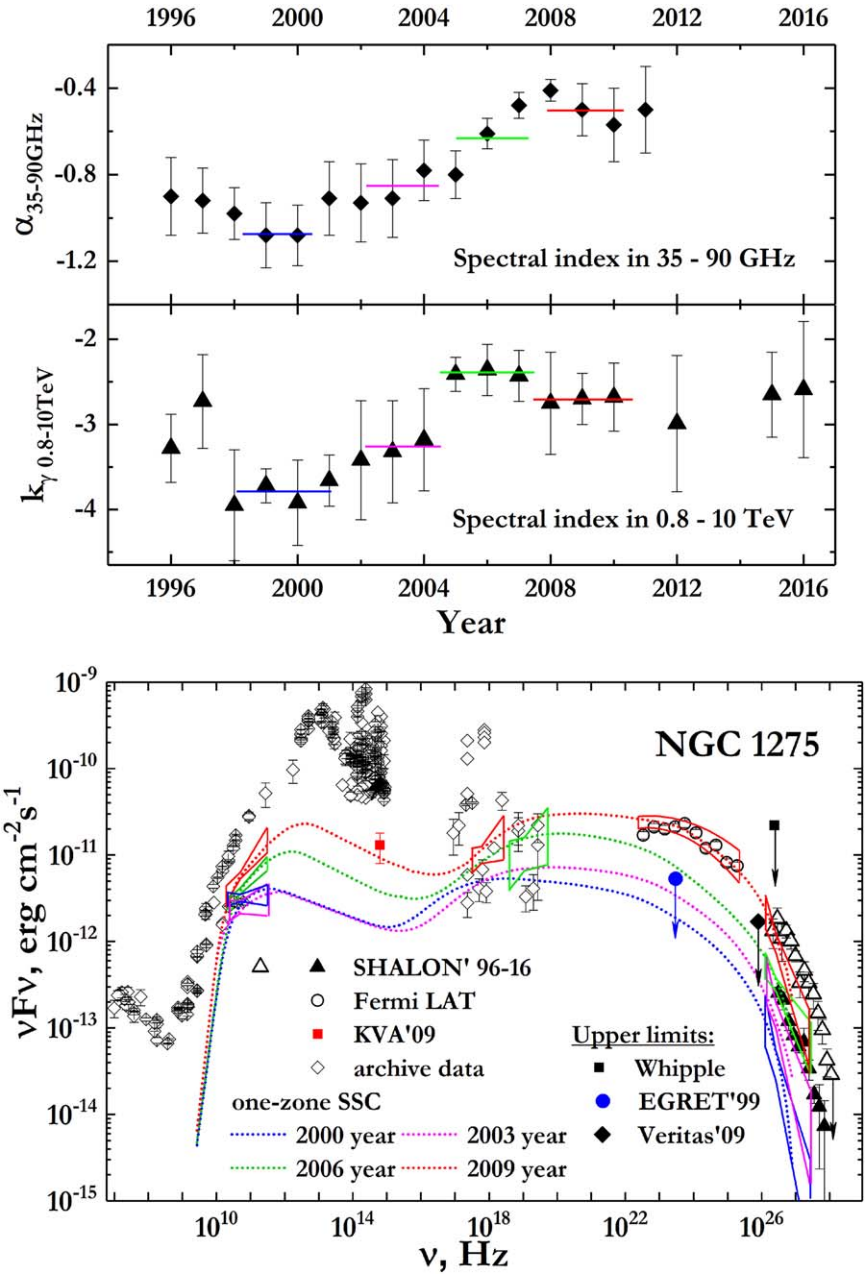

Figure 6. Top: The average power-law spectral index of NGC 1275, α between 35 and 90 GHz (K. L. Dutson et al. 2014), and k_γ between 0.8 and 10 TeV against time. Color lines show the value of spectral indices used for the one-zone synchrotron self-Compton modeling of spectral energy distribution evolution in time. Bottom: Spectral energy distribution of the γ-ray emission from NGC 1275. The points correspond to the long-term experimental data from Figure 1, right. The blue, magenta, green, and red bow tie areas are the spectra in the radio, X-ray, MeV–GeV, and TeV energy ranges taken in observations of 2000, 2003, 2006, and 2009, correspondingly. Green and red points are the data obtained in times near the observational times of the radio X-ray and TeV gamma-ray spectra. The blue, magenta, green, and red curves indicate the spectral energy distributions of NGC 1275 in 2000, 2003, 2006, and 2009 obtained in one-zone synchrotron self-Compton model.

emission is born by one spherical blob filled with nonthermal electrons propagating in the AGN jet with relativistic speeds. The model parameters are the blob radius R, its Doppler factor δ, and it is supposed to be filled by a homogeneous magnetic field B. The nonthermal electron energy distribution is assumed to be described by a broken power-law function. The physical parameters of the model applied here to fit the available data at radio, X-rays, and MeV–TeV gamma ray (bow tie areas in Figure 6) during the rising of activity are Doppler factor δ is in the range of 2.3–2.7, the magnetic field is $B = 0.045$–0.06 G, and the radius of the jet emission region is 2×10^{17} cm (0.026–0.065 pc). The indices of electrons' broken power law are in the range of $p1 = 2.1$–2.4 at $\gamma < \gamma_{\rm break}$, and index $p2 = 3.3$–3.6 at $\gamma > \gamma_{\rm break}$, where γ is the electron Lorentz factor, and its break value $\gamma_{\rm break}$ changes from 2.8 to 3.4. The minimum electron Lorentz factor is varied in the range 155–400, and its maximum value is from 3.5×10^6 to 10^7. The results of the modeling of the emission from NGC 1275 in 2000, 2003, 2006, and 2009 are shown in Figure 6, bottom with blue, magenta, green, and red lines, respectively. This model provides an adequate fit to the available NGC 1275 data during the period of rising fluxes and spectral evolution

observed in radio, X-ray, and high-, and very-high-energy gamma rays in 2000–2009.

4. Discussion

The intense investigations of the Perseus cluster and its central galaxy NGC 1275 through the wide range of the electromagnetic spectrum are contributing to an understanding of the physics of relativistic jets from AGNs. Also, as it was mentioned above, these studies are aiming to reveal the feedback role of the central galaxy, which was demonstrated in ROSAT and Chandra observations at low energies with the detections of the hot gas shells and cavities coinciding spatially with the radio structures originating in the central active part of the AGN (see H. Böhringer et al. 1993; E. Churazov et al. 2000; A. C. Fabian et al. 2000, 2006). The long-term observations of NGC 1275 at very-high energies resulted in the images of the galaxy and its surroundings (Figures 1, 2), flux, and spectral variations that suggested the origin of TeV gamma-ray emission in these regions is due to a number of processes.

The extended structures around NGC 1275 visible at energies of 800 GeV–55 TeV (Figure 1) are spatially coinciding with the X-ray emission regions and can be produced by mechanisms related to the generation of an X-ray structure (E. Churazov et al. 2000; A. C. Fabian et al. 2000, 2006). Both X-ray emission brightness distribution and the observed TeV emission show a sharp increase in intensity right outside the bubbles blown by the central black hole, which are visible in the radio band. This morphology together with the slow rise of intensity in the long-term variations, pointing to the increase of the particle density, suggests that the X-ray-generating particles are swept up from the region of the radio lobes under the pressure of cosmic rays and magnetic fields generated in the jets at the center of NGC 1275 (E. Churazov et al. 2000; A. C. Fabian et al. 2006). Thus, the formation of the structures visible in TeV gamma rays may occur through the interaction of very-high-energy cosmic rays with the gas inside the Perseus cluster and due to the heating of the interstellar gas at the boundary of the bubbles blown with increasing activity by the central black hole in NGC 1275.

Very-high-energy processes occurring in the region near the core of NGC 1275 are studied here first by the extracting of emission corresponding to the region of $\sim 32''$ around the nucleus. Also, the days-scale duration changes in the TeV gamma-ray fluxes were detected, which limits the size of the flaring region to about $\sim 10^{-3}$ pc depending on the Doppler factor. The detection of 1–40 TeV emission from the region of $\sim 32''$ around the position of NGC 1275 nucleus (see Figure 1, the black triangles) and the flux variability at the short-timescales (see also V. G. Sinitsyna & V. Y. Sinitsyna 2014) point to the origin of the part of very-high-energy emission due to the generation of jets ejected by the central SMBH in NGC 1275 at a parsec scale or even less region. But, as the angular resolution at the very-high energies is limited to tens of arcseconds, the exact location and size of the source of gamma rays cannot be found by the direct imaging way. Thus, the analysis of the light curves from multiwavelength long-term observations was made to reveal the cross correlations connecting with the relative location of the sources of emissions, and, in turn, to resolve the nuclear structure as viewed in different energies. First, to trace a possible common behavior, the TeV gamma-ray light curve as well as available data at X-ray data, and fluxes at radio frequencies, including 15, 37, 230, and 345 GHz, reflecting the activity of the AGN were considered. The light curves collected in the energy range from radio to very-high-energy gamma rays display both long-term and short-term variability of NGC 1275 emission. The inspection of the combined data at radio frequencies of 15, 37, 230, 345 GHz as well as X-ray data at 0.1–150 keV and gamma-ray fluxes at >100 MeV and >800 GeV energies shows the global trend of a gradual intensity increase starting from the period of 2003–2008. Earlier, before 2000, the drop in fluxes was observed in radio, soft X-rays, and TeV gamma rays (see Figure 4). But short-time TeV-flux increases were detected through all the periods of NGC 1275 observations, including the 1999–2003 period of the minimum intensity, which may be connected with formation of the many individual components (see Figure 4, the dashed lines) viewed in the radio wavelength at 43, 86 GHz (G. F. Paraschos et al. 2022). It was suggested (H. Nagai et al. 2010, 2012; K. Suzuki et al. 2012; K. L. Dutson et al. 2014; J. A. Hodgson et al. 2021) that the observed variations of the intensity could be driven by the complex behavior of inner core structures.

Monitoring of NGC 1275 at radio frequencies 43 GHz by VLBA shows that three radio-emission jet components C1, C2, C3 that exist near the nucleus account for the increase in the total flux at this frequency, at different time periods. The start of the activity increase in all ranges of the electromagnetic spectrum could be related to the appearance of these components. It is assumed that the C3 component is associated with the nucleus of NGC 1275 (H. Nagai et al. 2010, 2012), and the evolution of the C1 and C3 separation may be interpreted as C1 being launched from the nucleus between 2001 and 2003. Furthermore, the C2 jet component appeared in that period (K. Suzuki et al. 2012). Also, it is possible that C3 component coinciding with the NGC 1275 nucleus was unobservable before 2003 due to its inactivity. It should be noted that complex component behavior like changes in morphology interpreted as an additional new feature appearance is observed (J. A. Hodgson et al. 2021). The radio-emission regions were revealed with the multiband VLBI data, which is providing the opportunity to locate the gamma-ray emission region.

During the detailed analysis of the results of long-term observation of NGC 1275, it was found that very-high-energy gamma-ray emission significantly correlates with the collected radio fluxes (see Figure 5). Within the correlation analysis, it was found that the gamma-ray emission leads to the radio fluxes at 15, 37, 230, and 345 GHz by 2.03 ± 0.16, 1.93 ± 0.19, 1.88 ± 0.27, 1.84 ± 0.31 yr, respectively. Taking into account the higher-energy range considered in the study presented here, these values are consistent with ones obtained by G. F. Paraschos et al. (2023) for radio and Fermi-LAT gamma-ray light curves. The less pronounced positive time-lag of 1.89 ± 0.44 yr was found in the correlation analysis of 345 GHz and TeV gamma-ray light curve. Detecting both leading and lagging gamma rays may point to the presence of multiple gamma-ray-emitting sites in the source. It should be noted that depending on the location of the emitting structures, whether it is placed close to the black hole inside the broad-line region (BLR) or beyond it downstream of the jet, different models involving the inverse Compton scattering for the gamma-ray production are considered. The former relation of the radio and gamma-ray light curve corresponds to the

emission region located upstream of the radio core, at about (6.7–20.1) $\times$ 10^{-3} pc or (205.1–615.2)R_s, assuming the apparent jet speed and jet viewing angle subtracted from VLBI data by G. F. Paraschos et al. (2023). It places the gamma-ray emission site near the BLR, close to the central engine. Depending on the location of the black hole and jet base relative to the radio features, a part of gamma-ray emission preceding the radio fluxes can be associated with the C1 region. If the higher apparent speed of the VLBI features is assumed (B. Punsly et al. 2021; G. F. Paraschos et al. 2022), the location of the gamma-ray emitting region might be situated deeper to the black hole inside the BLR and point on the mechanism of the external inverse Compton on the seed photons of BLR zone (M. Sikora et al. 1994). The processes of multicomponent formation and jet bending, which were found to be occurring in the nucleus with the parameters revealed by B. Punsly et al. (2021) in the analysis of the NGC 1275 activity of 2018–2020, may ultimately lead to the production of the gamma rays in the region near the core of NGC 1275.

It is suggested in H. Nagai et al. (2010, 2016) that the source of the long-term increase of the fluxes was switched on by the launch of the C3 component located at $\leqslant$1 pc. Some of TeV gamma-ray emission comes trailing to the 345 GHz radio emission with the time-lag corresponding to the emission location of about (40.1–210.5) $\times$ 10^{-3} pc or (1224–6443)R_s at the direction of C3 component. As only a part of very-high-energy emission originates from around C3 region, the slower increase of the TeV fluxes compared with ones at radio and MeV–GeV gamma rays is observed. The correlation of X-ray and gamma-ray emissions with the about zero time-lag 0.13 $\pm$ 0.25 can be an evidence of the same location and the common origin of flares visible in these energy ranges.

The overall NGC 1275 spectral energy distribution is of a double-peaked shape and similar to that of a low-power blazar of the BL Lac object type. The one-zone SSC model that is widely used for the fitting of the SED of BL Lac objects was applied to describe both the overall collected data from NGC 1275 observations and spectral energy distribution changes during the period of gradual flux increase. To explain the radio, X-ray, and MeV–TeV gamma-ray spectral behavior during the gradual increase of activity in the period from 2000 to 2009 in the context of the one-zone SSC model, the maximum electron Lorentz factor would have changed from $\sim$4 $\times$ 10^6 up to $\sim$$10^7$, and about twice the growth of the minimum electron Lorentz factor from 158 to $\sim$400 is required. The gradual change of the index of power-law electron spectrum p1 from 2.1 to 2.4 (with only a slight variation of p2 in the range of 3.3–3.4) together with the increase of the break Lorentz factor from 630 to $\sim$2.5 $\times$ 10^3 is required. Also, to explain the observed growth of fluxes, the Doppler factor is required to increase from 2.3 to the 2.7 value. While the variation of the magnetic field is in the range of 0.045–0.06 G with the minimum of $B = 0.045$ G in 2003. The minimum values of the size of the emission region of 0.025 pc and the electron density of 45 cm^{-3} with a further increase up to 0.065 pc and 55 cm^{-3} are needed to fit the observed spectral changes. As a result, SSC model fits well the available NGC 1275 data corresponding to the spectral evolution of 2000–2009 observed in radio, X-ray, and MeV–TeV gamma rays. Although there is an uncertainty in the behavior of the optical fluxes including the period of 2000–2009, the tendency of the shift of the synchrotron peak frequency from the IR toward the visible light region may be traced. Meanwhile, the high-energy, SSC peak migrates from the hard X-ray energies of $\sim$3 $\times$ 10^{18} Hz to the region of high-energy gamma rays of $\sim$2 $\times$ 10^{21} Hz.

Also, the one-zone self-Compton is applied to NGC 1275 observational data, which was taken between 2008 and 2017 at the different states viewed in high energies in K. Tanada et al. (2018) considering the overall data at the low-energy range. The fit to the high- and very-high-energy part of spectral energy distribution data with the one-zone SSC model from K. Tanada et al. (2018) for the states of the period of SHALON observations is shown in Figure 1, right with the blue curve. The high-energy part of this model well fits the Fermi-LAT and SHALON data for the central region corresponding to the position of the nucleus of NGC 1275, whereas a significant deviation of the soft X-ray data from the model was shown (K. Tanada et al. 2018). As it was found in K. Tanada et al. (2018), it is difficult to describe the overall broadband spectral energy distribution considering a simple configuration of the core emission region with the one-zone SSC scenario presented (K. Tanada et al. 2018), but the more complicated emission region may be involved.

Given with the complex structure of the emitting region around the NGC 1275 viewed with radio data, the multi-component scenario was considered in S. Colafrancesco et al. (2010) for the description of the spectral energy distribution of the emission observed in the period since the 1990th. In this Cannon Model or CM model, a composition of the components of SSC emission from three different plasma blobs ejected from the inner regions of the NGC 1275 nucleus located close to the SMBH at a different time is considered. The multifrequency spectral energy distribution of emission from the nucleus of NGC 1275 from radio up to high and very-high energies is described in the frames of this model (see Figure 1, right, the dashed, dashed–dotted, and dashed–dotted with two-dot curves). Specifically, the available Fermi-LAT data at MeV–GeV energies and the high-energy part of the spectrum of the central region $<32''$ around the core of NGC 1275 from SHALON observations at TeV energies are described in terms of CM model with SSC emission of one of the blob-components, which is compact and most energetic with an electron population having the complex spectrum that originated from the nucleus itself (Figure 1, the dashed–dotted with two-dot curve). A larger radius blob-component produces an SSC emission that recovers the low-frequency radio emission and low flux X-ray data. But it was shown that to describe the X-ray part of the NGC 1275 spectral energy distribution including the various sets of historical data all three blob-components is required (S. Colafrancesco et al. 2010; see Figure 1, the dashed, dashed–dotted).

5. Conclusion

The most complete long-term observations across the electromagnetic spectrum from radio up to very-high-energy gamma rays are presented. The spectral energy distribution and emission maps obtained at a wide energy range show the connection of multiwavelength emission components whereas light curves provide evidence for the variability of NGC 1275 on decade timescales in the whole energy range.

The relation of the photon emission regions viewed in radio, X-rays to ones in very-high-energy gamma rays was found. The TeV gamma-ray emission regions observed by SHALON

from NGC 1275 well correlate with the features viewed in X-rays by Chandra and anticorrelate with radio structures. It was found that NGC 1275 structure in the TeV energy range is similar to the X-ray one and has an extended structure with a specific local maximum centered at a position of the core of the AGN. The emission component that corresponds to the contribution of the nucleus of NGC 1275 was identified, and its spectral energy distribution was extracted to obtain the characteristics of very-high-energy emission related to the core of NGC 1275.

It was found that the fluxes of X-rays, high-, and very-high-energy gamma rays as well as radio ones detected from the object have begun rising near the period of 2001–2003, which corresponds to the appearance of the relativistic jet features detected in radio 43 GHz viewed by VLA. Also, day-scale flux variations were detected at very-high energies in the whole period of observations. The analysis of the combined light-curve data shows that the radio and very-high-energy gamma-ray fluxes are correlated, and predominantly, the gamma rays lead the radio emission. The constraints on the possible locations of the source of gamma rays in the NGC 1275 relative to the central black hole engine are put forth.

The evolution of the NGC 1275 spectral energy distribution, caused possibly by the appearance of jet features as viewed by VLA, was considered. The one-zone self-Compton model was applied to describe the SED evolution during the rise of the fluxes in the period from 2000 to 2009. The modeling of the evolving SED assumes that the gradual flux and spectral changes detected with the broadband long-term observations may be mostly caused by injection of high-energy electrons into the jet with the growth of the value of the break in the electron Lorentz factor together with a changing Doppler factor within the emission region of <0.065 pc. Also, the SSC fit to the overall spectral energy distribution is presented. The high-energy part of the overall SSC modeling fits well the Fermi-LAT and SHALON data corresponding to the central region related to the NGC 1275 core location. But there is a significant deviation of the soft X-ray data from this model. The scenario that considers the more complicated mechanism involving three radio-emission jet components demonstrates a better agreement with overall spectral energy distribution data.

The data obtained at GeV–TeV energies show that high- and very-high-energy emission are generated by several processes. A part of this emission is generated in the nucleus of NGC 1275 by relativistic jets. An extended structure around NGC 1275 detected in X-rays and gamma rays points to the production of gamma-ray emission due to the interaction of cosmic rays and magnetic fields generated in the jets at the galactic center with the gas of the Perseus cluster.

Acknowledgments

The authors would like to thank the referee for the valuable comments and suggestions to improve the manuscript.

Appendix A
Details of Very-high-energy Spectral Energy Distributions

Table 1 gives the spectral energy distribution points corresponding to the open triangles in Figure 1, right and Figure 6, obtained in the long-term observations by SHALON in the energy range 0.8–55 TeV, and the signal detection confidence level according to Li–Ma formulation (T.-P. Li & Y.-Q. Ma 1983) in each energy interval.

Table 2 gives the spectral energy distribution points of the peak of gamma-ray intensity of $\sim 32''$ size around the position of the NGC 1275 core (▲ triangles in Figure 1, right and Figure 6), obtained in the long-term observations by SHALON in the energy range 1–40 TeV, and the signal detection confidence level according to Li–Ma formulation (T.-P. Li & Y.-Q. Ma 1983) in each energy interval.

Table 1
NGC 1275 Spectral Energy Distribution Information in the Energy Range 0.8–55 TeV

E (TeV)	σ (T.-P. Li & Y.-Q. Ma 1983)	νF_ν (erg cm^{-2} s^{-1})
0.88	8.9	$(1.32 \pm 0.26) \times 10^{-12}$
1.19	11.5	$(1.85 \pm 0.22) \times 10^{-12}$
1.62	9.5	$(1.08 \pm 0.14) \times 10^{-12}$
2.19	10.1	$(1.31 \pm 0.17) \times 10^{-12}$
2.97	15.4	$(1.01 \pm 0.11) \times 10^{-12}$
4.03	10.3	$(6.78 \pm 1.08) \times 10^{-13}$
5.47	8.3	$(3.34 \pm 0.61) \times 10^{-13}$
7.41	8.1	$(4.63 \pm 0.92) \times 10^{-13}$
11.0	7.2	$(3.31 \pm 0.88) \times 10^{-13}$
13.6	6.9	$(2.46 \pm 0.76) \times 10^{-13}$
18.5	5.1	$(1.48 \pm 0.54) \times 10^{-13}$
25.0	4.3	$(9.52 \pm 3.23) \times 10^{-14}$
33.8	3.0	$(4.23 \pm 1.81) \times 10^{-14}$
45.9	1.4	$(2.88 \pm 2.70) \times 10^{-14}$

Table 2
NGC 1275 Spectral Energy Distribution Information in the Energy Range 1–40 TeV

E (TeV)	σ (T.-P. Li & Y.-Q. Ma 1983)	νF_ν (erg cm^{-2} s^{-1})
1.24	5.7	$(2.54 \pm 0.71) \times 10^{-13}$
1.42	7.0	$(2.09 \pm 0.39) \times 10^{-13}$
2.53	9.8	$(1.19 \pm 0.15) \times 10^{-13}$
3.57	6.4	$(8.16 \pm 1.21) \times 10^{-14}$
5.04	8.9	$(6.11 \pm 1.10) \times 10^{-14}$
7.15	7.2	$(6.91 \pm 1.32) \times 10^{-14}$
10.1	4.9	$(3.37 \pm 0.84) \times 10^{-14}$
14.3	3.6	$(1.71 \pm 0.42) \times 10^{-14}$
20.1	2.4	$(1.22 \pm 0.58) \times 10^{-14}$
28.4	1.2	$(7.31 \pm 6.57) \times 10^{-15}$

Appendix B
Details of Light Curves for NGC 1275 at Very-high Energies ($E > 800$ GeV)

Table 3 gives the year-averaged light-curve points corresponding to the red triangles in Figure 4, top, obtained in the long-term observations by SHALON in the energy range 0.8–55 TeV, and the signal detection confidence level according to T.-P. Li & Y.-Q. Ma (1983).

Table 4 gives the points of the detailed light curve presented using the yellow-filled triangles in Figure 4, top, which were obtained in the long-term observations by SHALON in the energy range 0.8–55 TeV, together with the signal detection confidence level according to T.-P. Li & Y.-Q. Ma (1983).

Table 3
Information about NGC 1275 Year-averaged Light Curve Collected in the Energy Range 0.8–55 TeV

Date	$I(>0.8$ TeV) (ph cm^{-2} s^{-1})	σ (T.-P. Li & Y.-Q. Ma 1983)
1996.5	$(8.49 \pm 1.20) \times 10^{-13}$	6.67
1997.5	$(7.43 \pm 0.85) \times 10^{-13}$	5.81
1998.5	$(9.35 \pm 2.60) \times 10^{-13}$	6.1
1999.5	$(4.34 \pm 0.83) \times 10^{-13}$	5.92
2000.5	$(3.45 \pm 0.80) \times 10^{-13}$	3.74
2001.5	$(5.52 \pm 1.40) \times 10^{-13}$	5.98
2002.5	$(3.90 \pm 2.30) \times 10^{-13}$	2.73
2003.5	$(7.71 \pm 1.30) \times 10^{-13}$	8.51
2004.5	$(5.27 \pm 1.10) \times 10^{-13}$	5.3
2005.5	$(5.63 \pm 0.91) \times 10^{-13}$	8.29
2006.5	$(7.31 \pm 1.40) \times 10^{-13}$	6.82
2007.5	$(6.18 \pm 1.10) \times 10^{-13}$	6.22
2008.5	$(9.06 \pm 1.50) \times 10^{-13}$	6.39
2009.5	$(12.5 \pm 1.70) \times 10^{-13}$	11.08
2010.5	$(15.1 \pm 5.30) \times 10^{-13}$	5.17
2012.5	$(11.2 \pm 3.50) \times 10^{-13}$	5.02
2015.5	$(14.5 \pm 3.01) \times 10^{-13}$	5.28
2016.5	$(9.54 \pm 1.90) \times 10^{-13}$	5.13

Table 4
Information about NGC 1275 Detailed Light Curve Collected in the Energy Range 0.8–55 TeV

Date	$I(>0.8$ TeV) (ph cm^{-2} s^{-1})	σ (T.-P. Li & Y.-Q. Ma 1983)
1996.7049	$(10.2 \pm 4.3) \times 10^{-13}$	4.22
1996.7787	$(3.91 \pm 1.8) \times 10^{-13}$	2.75
1996.8661	$(7.98 \pm 2.5) \times 10^{-13}$	3.85
1997.9726	$(9.20 \pm 3.8) \times 10^{-13}$	4.81
1997.9973	$(5.33 \pm 1.8) \times 10^{-13}$	4.22
1998.077	$(3.80 \pm 1.5) \times 10^{-13}$	1.1
1998.13	$(5.90 \pm 2.5) \times 10^{-13}$	1.89
1999.126	$(5.79 \pm 1.4) \times 10^{-13}$	4.76
1999.6849	$(6.93 \pm 2.1) \times 10^{-13}$	3.74
1999.7096	$(1.80 \pm 0.9) \times 10^{-13}$	1.94
1999.7698	$(4.80 \pm 0.12) \times 10^{-13}$	3.07
2000.6721	$(4.10 \pm 1.8) \times 10^{-13}$	3.11
2000.9645	$(2.11 \pm 1.05) \times 10^{-13}$	2.65
2001.0767	$(12.4 \pm 3.5) \times 10^{-13}$	6.15
2001.7123	$(1.68 \pm 0.79) \times 10^{-13}$	1.95
2002.926	$(3.10 \pm 0.89) \times 10^{-13}$	1.92
2003.7479	$(10.8 \pm 3.5) \times 10^{-13}$	5.13
2003.8164	$(3.53 \pm 0.91) \times 10^{-13}$	2.44
2003.9068	$(6.13 \pm 0.72) \times 10^{-13}$	3.14
2003.9178	$(8.38 \pm 1.2) \times 10^{-13}$	4.21
2003.9699	$(5.24 \pm 1.5) \times 10^{-13}$	4.38
2004.7186	$(12.1 \pm 4.1) \times 10^{-13}$	4.53
2004.877	$(3.27 \pm 1.1) \times 10^{-13}$	1.99
2004.929	$(6.58 \pm 2.3) \times 10^{-13}$	3.08
2005.6822	$(5.20 \pm 2.0) \times 10^{-13}$	2.1
2005.7644	$(7.42 \pm 2.2) \times 10^{-13}$	4.04
2005.8219	$(4.15 \pm 1.0) \times 10^{-13}$	3.11
2005.8466	$(5.71 \pm 1.3) \times 10^{-13}$	4.61
2005.9178	$(16.5 \pm 5.1) \times 10^{-13}$	5.47
2006.7288	$(6.10 \pm 3.2) \times 10^{-13}$	2.71
2006.8164	$(10.8 \pm 3.5) \times 10^{-13}$	5.62
2006.8877	$(6.90 \pm 1.9) \times 10^{-13}$	3.28
2006.9699	$(8.16 \pm 2.02) \times 10^{-13}$	4.09
2007.0384	$(5.40 \pm 1.2) \times 10^{-13}$	3.43
2007.0548	$(6.80 \pm 3.02) \times 10^{-13}$	2.42
2007.126	$(9.30 \pm 3.1) \times 10^{-13}$	3.34
2007.7808	$(4.84 \pm 1.3) \times 10^{-13}$	4.11
2008.8415	$(9.64 \pm 2.3) \times 10^{-13}$	4.31

Table 4
(Continued)

Date	$I(>0.8$ TeV) (ph cm^{-2} s^{-1})	σ (T.-P. Li & Y.-Q. Ma 1983)
2008.9044	$(8.83 \pm 2.4) \times 10^{-13}$	4.92
2009.7918	$(12.1 \pm 3.3) \times 10^{-13}$	6.34
2009.8027	$(16.4 \pm 3.04) \times 10^{-13}$	7.92
2009.8164	$(24.3 \pm 6.4) \times 10^{-13}$	4.11
2009.863	$(12.4 \pm 4.2) \times 10^{-13}$	3.92
2010.8603	$(11.2 \pm 5.1) \times 10^{-13}$	4.18
2010.9151	$(18.7 \pm 6.1) \times 10^{-13}$	4.79
2012.8005	$(8.53 \pm 4.2) \times 10^{-13}$	3.65
2012.8716	$(14.5 \pm 6.7) \times 10^{-13}$	3.71
2015.7068	$(16.5 \pm 5.3) \times 10^{-13}$	4.92
2015.7753	$(6.63 \pm 3.2) \times 10^{-13}$	3.85
2016.8224	$(8.18 \pm 3.5) \times 10^{-13}$	4.51
2016.8443	$(11.8 \pm 4.7) \times 10^{-13}$	4.71

References

Abdo, A. A., Ackermann, M., Ajello, M., et al. 2009, ApJ, 699, 31
Acciari, V. A., Aliu, E., Arlen, T., et al. 2009, ApJL, 706, L275
Acero, F., Ackermann, M., Ajello, M., et al. 2015, ApJS, 218, 23
Ackermann, M., Ajello, M., Atwood, W. B., et al. 2016, ApJS, 222, 5
Aléksic, J., Antonelli, L. A., Antoranz, P., et al. 2010, ApJ, 710, 634A
Amenomori, M. 1999, ICRC (Salt Lake City), 3, 418
Angel, J. R. P., & Stockman, H. S. 1980, ARA&A, 18, 321
Asada, K., Kameno, S., Shen, Z.-Q., et al. 2006, PASJ, 58, 261
Asada, K., Kameno, S., Shen, Z.-Q., et al. 2009, in ASP Conf. Ser. 402, Approaching Micro-Arcsecond Resolution with VSOP-2, ed. Y. Hagiwara et al. (San Francisco, CA: ASP), 91A
Atwood, W. B., Abdo, A. A., Ackermann, M., et al. 2009, ApJ, 697, 1071
Blandford, R. D., & Königl, A. 1979, ApJ, 232, 34
Blandford, R. D., Meier, D., & Readhead, A. 2019, ARAA, 57, 467
Böhringer, H., Voges, W., Fabian, A. C., Edge, A. C., & Neumann, D. M. 1993, MNRAS, 264, L25
Brown, A. M., & Adams, J. 2011, MNRAS, 413, 2785
Chidiac, C., Rani, B., Krichbaum, T. P., Angelakis, E., et al. 2016, A&A, 590, A61
Colafrancesco, S., & Blasi, P. 1998, APh, 9, 227
Colafrancesco, S., & Marchegiani, P. 2009, A&A, 502, 711
Colafrancesco, S., Marchegiani, P., & Giommi, P. 2010, A&A, 519, A82
Connolly, S. 2015, arXiv:1503.06676
Churazov, E., Forman, W., Jones, C., & Böhringer, H. 2000, A&A, 356, 788
Dutson, K. L., Edge, A. C., Hinton, J. A., et al. 2014, MNRAS, 442, 2048
Dennison, B. 1980, ApJL, 239, L93
Edahiro, I., Fukazawa, Y., Kawaguchi, K., Tanaka, Y., et al. 2015, arXiv:1503.02890
Edelson, R. A., & Krolik, J. H. 1988, ApJ, 333, 646
Emmanoulopoulos, D., McHardy, I. M., & Papadakis, I. E. 2013, MNRAS, 433, 907
Fabian, A. C., Sanders, J. S., Ettori, S., et al. 2000, MNRAS, 318, L65
Fabian, A. C., Sanders, J. S., Taylor, G. B., et al. 2006, MNRAS, 366, 417
Fabian, A. C., Walker, S. A., Pinto, C., Russell, H. R., & Edge, A. C. 2015, MNRAS, 451, 3061
Fanaroff, B. L., & Riley, J. M. 1974, MNRAS, 167, 31P
Forston, L. 2019, in Proc. Rencontres de Blois 31, 20
Fossati, G., Maraschi, L., Celotti, A., Comastri, A., & Ghisellini, G. 1998, MNRAS, 299, 433
Fukazawa, Y., Shiki, K., Tanaka, Y., et al. 2018, ApJ, 855, 93
Gallagher, J. S. 2009, AN, 220, 1040G
Gendron-Marsolais, M., Hlavacek-Larrondo, J., van Weeren, R. J., et al. 2020, MNRAS, 499, 5791
Goncharskii, A. V., Cherepashchuk, A. M., & Yagola, A. G. 1985, On Some Problems of Astrophysics (Washington, DC: NASA), 250
Gurwell, M. A., et al. 2007, in ASP Conf. Ser., 375, From Z-Machines to ALMA, ed. A. J. Baker et al. (San Francisco, CA: ASP), 234
Hodgson, J. A., Rani, B., Oh, J., Marscher, A., et al. 2021, ApJ, 914, 43
Houston, B. P., Wolfendale, A. W., & Young, C. M. 1984, JPhG, 10, L147
Imazato, F., Fukazawa, Y., Mahito, S., & Sakamoto, T. 2021, ApJ, 906, 30
Inoue, S., & Takahara, F. 1996, ApJ, 463, 555
Jorstad, S. G., Marscher, A. P., Larionov, V. M., et al. 2010, ApJ, 715, 362
Jorstad, S. G., Marscher, A. P., Smith, P. S., et al. 2013, ApJ, 773, 147
Kharb, P., Lister, M. L., & Cooper, N. J. 2010, ApJ, 710, 764K
Kingham, K. A., & Oconnell, R. W. 1979, AJ, 84, 1537
Koljonen, K. I. I., Maccarone, T., McCollough, M. L., et al. 2018, A&A, 612, A27
Königl, A. A. 1981, ApJ, 243, 700
Kravchenko, E. V., Kovalev, Y. Y., Hovatta, T., & Ramakrishnan, V. 2016, MNRAS, 462, 2747
Kubo, H., Takahashi, T., Madejski, G., et al. 1998, ApJ, 504, 693
Li, T.-P., & Ma, Y.-Q. 1983, ApJ, 272, 317
Liu, F. K., & Chen, X. 2007, ApJ, 671, 1272
Lobanov, A. P. 1998, A&A, 330, 79
Lyutyi, V. M. 1977, SvA, 21, 655
Miniati, F. T., Jones, T. W., Kang, H., & Ryu, D. 2001, ApJ, 62, 233
McNamara, B. R., & Nulsen, P. E. J. 2012, NJPh, 14, 055023
Moseiko, N. I., Klimov, A. I., Sinitsyna, V. G., et al. 2020, NIMPA, 952, 161755
Nagai, H., Chida, H., Kino, M., Orienti, M., et al. 2016, AN, 337, 69
Nagai, H., Orienti, M., Kino, M., et al. 2012, MNRAS, 423, L122
Nagai, H., Suzuki, K., Asada, K., et al. 2010, PASJ, 62, L11
Nikolsky, S. I., & Sinitsyna, V. G. 1989, in Proc. of the Int. Workshop of Very-high Energy Gamma-Ray Astronomy, ed. A. A. Stepanian, D. J. Fegan, & W. F. Cawley (Dublin: Univ. College), 11
Nikolsky, S. I., & Sinitsyna, V. G. 2003, NuPhS, 122, 409
Nikolsky, S. I., & Sinitsyna, V. G. 2004, PAN, 67, 1900
Paraschos, G. F., Kim, J. Y., Krichbaum, T. P., & Zensus, J. A. 2021, A&A, 650, L18
Paraschos, G. F., Krichbaum, T. P., Kim, J.-Y., et al. 2022, A&A, 665, A1
Paraschos, G. F., Mpisketzis, V., Kim, J.-Y., et al. 2023, A&A, 669, A32
Pedlar, A., Ghataure, H. S., Davies, R. D., et al. 1990, MNRAS, 246, 477
Perkins, J. S., Badran, H. M., Blaylock, G., et al. 2006, ApJ, 644, 148
Punsly, B., Nagai, H., Savolainen, T., & Orienti, M. 2021, ApJ, 911, 19
Pushkarev, A. B., Kovalev, Y. Y., & Lister, M. L. 2010, ApJL, 722, L7
Reimer, O., Pohl, M., Sreekumar, P., & Mattox, J. R. 2003, ApJ, 588, 155
Robertson, D. R. S., Gallo, L. C., Zoghbi, A., & Fabian, A. C. 2015, MNRAS, 453, 3455
Sarazin, C. L. 1999, ApJ, 520, 529
Sikora, M., Begelman, M. C., & Rees, M. J. 1994, ApJ, 421, 153
Sikora, M., Stawarz, Ł., Moderski, R., Nalewajko, K., & Madejski, G. M. 2009, ApJ, 704, 38
Sinitsyna, V. G. 1993, in Proc. the Int. Workshop Toward a Major Atmospheric Cherenkov Detector - II, ed. R. C. Lamb (Ames, IA: Iowa State Univ.), 91
Sinitsyna, V. G. 1995, in Proc. of the Int. Workshop Toward a Major Atmospheric Cherenkov Detector IV, ed. M. Cresti (Padua: Papergraf), 133
Sinitsyna, V. G. 1996, NCimB, 19, 965
Sinitsyna, V. G. 1997, in Proc. of the Int. Workshop, Toward a Major Atmospheric Cherenkov Detector V, ed. O. De Jager (Potchefstroom: Westprin), 136
Sinitsyna, V. G. 2000, in AIP Conf. Proc. 515, GeV-TeV GAMMA RAY ASTROPHYSICS WORKSHOP: Towards a Major Atmospheric Cherenkov Detector VI *(Snowbird, Utah, USA)* (Melville, NY: AIP), 293
Sinitsyna, V. G. 2006, RaPC, 75, 880
Sinitsyna, V. G., Alaverdian, A. Y., Arsov, T. P., et al. 1999, NuPhS, 75A, 352
Sinitsyna, V. G., Alaverdian, A. Y., Borisov, S. S., Nikolsky, S. I., & Sinitsyna, V.Y. 2011, in Proc. 12th ICATPP Cosmic Rays For Particle and Astroparticle Physics, 6, ed. S. Giani, C. Leroy, & P. G. Rancoita (Como: World Scientific), 296
Sinitsyna, V. G., Arsov, T. P., Borisov, S.S., et al. 2007, BRASP, 71, 906
Sinitsyna, V. G., Mirzafatikhov, R. M., Musin, F. I., et al. 2009, NuPhS, 196, 442
Sinitsyna, V. G., & Sinitsyna, V. Y. 2011, AstL, 37, 621
Sinitsyna, V. G., & Sinitsyna, V. Y. 2013, in EPJ Web of Conf.: XVII International Symposium on Very High Energy Cosmic Ray Interactions, ed. U. Gensch & M. Walter (Les Ulis: EDP Sciences), 10005
Sinitsyna, V. G., & Sinitsyna, V. Y. 2014, AstL, 40, 91
Sinitsyna, V. G., & Sinitsyna, V. Y. 2020, JPhCS, 1468, 012086
Sinitsyna, V. G., & Sinitsyna, V. Y. 2022, Univ, 8, 57
Sinitsyna, V. G., Sinitsyna, V. Y., Borisov, S. S., et al. 2018, AdSpR, 62, 2845
Sinitsyna, V. G., Sinitsyna, V. Y., Borisov, S. S., et al. 2020, NIMPA, 952, 161775
Strauss, M., Huchra, J. P., Davis, M., et al. 1992, ApJS, 83, 29S
Strong, A. W., & Bignami, G. F. 1983, ApJ, 274, 549
Suzuki, K., Nagai, H., Kino, M., et al. 2012, ApJ, 746, 140
Tanada, K., Kataoka, J., Arimoto, M., et al. 2018, ApJ, 860, 74

Taylor, G. B., & Vermeulen, R. C. 1996, ApJL, 457, L69
Teräsranta, H., Tornikoski, M., Mujunen, A., et al. 1998, A&AS, 132, 305
Teräsranta, H., Wiren, S., Koivisto, P., et al. 2005, A&A, 440, 409
Timokhin, A. N. 2004, A&A, 417, 391
Thompson, D. J., Bertsch, D. L., Dingus, B. L., et al. 1995, ApJS, 101, 209
Tramacere, A., Giommi, P., Perri, M., Verrecchia, F., & Tosti, G. 2009, A&A, 501, 879
Urry, C. M., & Padovani, P. 1995, PASP, 107, 803
Vaughan, S. 2005, A&A, 431, 391
Vermeulen, R. C., Readhead, A. C. S., & Backer, D. C. 1994, ApJ, 430, L41
Veron-Cetty, M. P., & Veron, P. 1998, yCat, VII/207
Wilman, R. J., Edge, A. C., & Johnstone, R. M. 2005, MNRAS, 359, 755
Yamazaki, S., Fukazawa, Y., Sasada, M., et al. 2013, PASJ, 65, 30
Zdziarski, A. A., Sikora, M., Dubus, G., et al. 2012, MNRAS, 421, 2956